Mineral cathodic electro-precipitation and its kinetic modelling in thin-film microfluidic reactor during advanced electro-oxidation process

Faidzul Hakim Adnan, Emmanuel Mousset, Steve Pontvianne, Marie-Noëlle Pons

Mineral cathodic electro-precipitation and its kinetic modelling in thin-film microfluidic reactor during advanced electro-oxidation process

Faidzul Hakim ADNAN[1], Emmanuel MOUSSET[1,*], Steve PONTVIANNE[1], Marie-Noëlle PONS[1,2]

[1] *Laboratoire Réactions et Génie des Procédés, Université de Lorraine, CNRS, LRGP, F-54000 Nancy, France*
[2] *LTSER-LRGP, CNRS, Université de Lorraine, F-54000 Nancy, France*

ACCEPTED IN

***ELECTROCHIMICA ACTA* JOURNAL**

(Special Issue from ISE Belgrade online meeting 2020 - Symposium 12)

FOR CONSIDERATION

*Contact of corresponding author: emmanuel.mousset@cnrs.fr

HIGHLIGHTS

- Local cathodic alkalization occurs predominantly due to H_2O reduction not O_2
- Electromigration does not influence electro-precipitation within the conditions
- $Mg(OH)_2$ electro-precipitation depends only on applied current density
- Gas evolution and Mg^{2+} ion decrease $CaCO_3$ electro-precipitation
- Models to predict electro-precipitation in thin-film cell have been proposed

ABSTRACT

It is presented for the first time the occurrence and modelling of cathodic mineral electro-precipitation in microfluidic thin-film configuration of electrochemical advanced oxidation process (EAOP), in order to better understand and predict the cathode's scaling when treating water containing Mg^{2+} and Ca^{2+}. Upon a systematic study, the main results show that when an inter-electrode distance of 500 μm is used at 4 mA cm^{-2}, local alkalization on cathode surface occurs despite the absence of dissolved O_2 suggesting that it takes place due predominantly to water reduction (current efficiency > 99%) and not dissolved O_2 reduction. Moreover, electromigration phenomenon could be neglected when varying ionic strength from 0.02 to 0.1 mol L^{-1}, while diffusion was the kinetic rate-limiting step. In addition, $Ca(OH)_2$ and $MgCO_3$ precipitates were not formed under all investigated conditions. $Mg(OH)_2$ electro-precipitation was found to be highly dependent on current density, but independent of other ionic species jointly present in electrolyte. $Mg(OH)_2$ precipitated once interfacial pH of 10.2 was reached. More $CaCO_3$ was electro-precipitated at lower current density (ca. 7.2%) owing to more vigorous gas evolution when higher current density was applied. 12% less $CaCO_3$ electro-precipitation was found in the presence of Mg^{2+} confirming its inhibiting effect towards $CaCO_3$ scaling. The mathematical model proposed could fit well the experimental curves (Root mean square error (RMSE) < 0.1163) and permit to predict the evolution of concentration of depositing species (i.e. Mg^{2+}, Ca^{2+} and CO_3^{2-}). Furthermore, the role of hydroxyl radicals ($^{\bullet}OH$) produced at boron-doped diamond (BDD) anode could be neglected upon the applied conditions, meaning that the outcome of this study is reliable across all types of water containing Mg^{2+}, Ca^{2+} and/or CO_3^{2-} in compliance to their ubiquity when it is to be treated by electrolysis in general.

Keywords: advanced oxidation process, electro-oxidation, electro-precipitation, microfluidic, scaling

1. Introduction

Occurrence of bio-recalcitrant pollutants in the effluent of municipal or industrial wastewater treatment plants (WWTPs) has been raising concerns amongst different stakeholders in the field of environment and ecology. More and more organic pollutants traceable in the wastewater have been categorized as emerging pollutants due to their recalcitrance property and potential toxicity to living organisms [1, 2]. In the objective of elimination of persistent pollutants in aquatic environment and for water reuse purpose, additional treatment to the effluent of WWTPs seems obligatory. A variety of supplementary treatments has been proposed across literature and the majority of them are based on the fundamentals of chemical oxidation where strong oxidants are involved in the degradation of pollutants. Classical processes such as chlorination, ozonation and advanced oxidation processes (AOPs) (e.g. ozonation, peroxonation, heterogeneous photocatalysis and (photo)-Fenton processes) are to some extent well established to degrade effectively contaminants in aqueous media [3]. Nevertheless, their efficiency comes with firstly high price tag [4] and secondly the prerequisite of adding chemical reagents into the media to be treated.

Electrochemical advanced oxidation processes (EAOPs) have also been reported to remove recalcitrant organic pollutants [5, 6]. A huge boost to the AOPs is that EAOPs do not necessarily require the addition of chemical reagents since strong hydroxyl radical oxidants (•OH) are electrogenerated continuously in-situ [7]. Owing to the development of diamond-based anode, higher degree of electrochemical oxidation of organic contaminants has been reached [8, 9]. Furthermore, the application of microfluidic reactor within the framework of EAOPs has spurred the capability of wastewater treatment [10-14]. It allows mineralization of organic pollutants without the addition of supporting electrolyte. The micrometric inter-electrode distance vastly accommodates the phenomenon of limitation by mass transfer and ohmic resistance [15] in the case of effluent having relatively low ionic conductivity [16].

In spite of that, there is a major drawback within the application of EAOPs and more generally electrolysis to treat wastewater. While treating water of varying concentrations of calcium (Ca^{2+}) and magnesium (Mg^{2+}) ions), a layer of insulating deposit can be formed on the surface of cathode. Despite low concentration of Ca^{2+} and Mg^{2+} in an effluent, in case of the operation of electrochemical cells in continuous-mode such, most of the time, encountered in industrial applications, the deposit progressively passivates the whole electrode surface. Sequencing polarity inversion might be applied as counter-measure but it might take a toll on treatment efficacy, duration of operation and overall operational cost. Furthermore, cathode in operation must be able to tolerate high anodic current during the inverted polarization step given the fact that some cathode materials have been reported to be corroded in such conditions **[17]**. Upon treating water with high Ca^{2+} and Mg^{2+} content, sequencing inversion of polarity might not be the best strategy since the passivation of electrode occurs anyhow. Eventually, without regular intervention, electrochemical cells become very inefficient or probably are no longer operational.

The mechanism of formation of deposits has been well established in the literature **[18, 19]**. When the electrode is polarized at a sufficiently negative potential, dissolved oxygen (O_2) is reduced to hydroxide ions (OH^-) according to **Eq. (1)**, resulting in an increase of local pH **[20, 21]**.

$$O_2 + 2H_2O + 4e^- \rightarrow 4OH^- \quad (1)$$

At a more cathodic potential, reduction of solvent (H_2O) can take place according to **Eq. (2)** which also produces hydroxide ions as well as hydrogen gas (H_2).

$$2H_2O + 2e^- \rightarrow H_2 + 2OH^- \quad (2)$$

As shown in **Eqs. (3)-(4)**, in the presence of Mg^{2+} and Ca^{2+}, deposits of hydroxide can be produced. Moreover, the pH increment also shifts thermodynamic ratio of carbonates/bicarbonates (**Eq. (5)**) favoring the production of carbonate scales as written in **Eqs. (6)-(7)**.

$$Mg^{2+} + 2OH^- \leftrightarrow Mg(OH)_2 \quad (3)$$

$$Ca^{2+} + 2OH^- \leftrightarrow Ca(OH)_2 \quad (4)$$

$$OH^- + HCO_3^- \leftrightarrow H_2O + CO_3^{2-} \quad (5)$$

$$Ca^{2+} + CO_3^{2-} \leftrightarrow CaCO_3 \quad (6)$$

$$Mg^{2+} + CO_3^{2-} \leftrightarrow MgCO_3 \quad (7)$$

Different studies have already demonstrated the formation of aforementioned deposits in electrochemical cell while operating with different types of water with varying contents of Ca^{2+} and Mg^{2+}. They are characterized by their source and application domain: synthetic water for cooling system in cooling towers and oil refineries **[22, 23]**, artificial **[24, 25]** and natural groundwater **[26, 27]**, mineral potable water **[28, 29]**, artificial **[19, 30-32]** and real seawater **[33, 34]**. Interestingly, the reported works were all conducted on the classical rotating disk electrode (RDE) possessing effective exposed surface area of 0.2 cm^2 **[19, 24-28, 30, 33]**, 0.5 cm^2 **[22, 23, 35]**, 1 cm^2 **[32, 36, 37]** and 1.5 cm^2 **[31]**. Either carbon steel, gold or stainless steel was used as the working electrode playing the role of cathode. To the best of authors' knowledge, the study of electro-precipitation outside aforementioned configuration is scarce.

Due to the omnipresence of calcium and magnesium in water, further study to understand and more particularly to avoid the formation of insulating deposition at larger scale seems primordial. It is within this context that a detailed investigation has been carried out to understand the influence of electrolytic composition towards the formation of mineral deposits on electrode surface during EAOP. The objective is to establish operating conditions in-which scaling does not occur, or, is minimized owing to the benefits attributed by a microfluidic cell. Moreover, addition of chemical reagents is no longer compulsory in micro-reactor; hence, interference possibly originating from the supporting electrolyte is avoided. Magnesium hydroxide ($Mg(OH)_2$), calcium carbonate ($CaCO_3$) and

magnesium carbonate ($MgCO_3$) deposits are studied due to the ubiquity of Mg^{2+}, Ca^{2+} and HCO_3^- /CO_3^{2-} ions in water sources. Results presented in this paper are the first to elucidate the phenomenon of passivation in microfluidic reactor, a configuration very distinctive to those reported in the literature where RDE were used as working electrode. The geometry and configuration of microfluidic cell adopted in this work are closely representative to reactors used in industries. Notably, the difference between electrode surface in this present study is 25 to 250 times bigger compared to RDEs (0.2 to 2 cm^2) used in the literature. The present design is more adapted for further applications on a larger scale. Synthetic water is used in this work, but it closely mimics the average characteristic of effluent of municipal WWTPs particularly the concentration of Ca^{2+}, Mg^{2+} and carbonates as well as pH and ionic conductivity. Furthermore, it is the first time that the influence on electro-precipitation of hydroxyl radicals produced at high O_2 evolution overvoltage anode is studied. Novel theoretical models are developed in this paper where the objectives are two-fold; first, assumptions made to establish the models lead to a better understanding of the mechanism of mineral electro-precipitation if they occur. Second, these models are the first to be reported to predict the evolution of electro-precipitating ions, particularly under the configuration of thin-film microfluidic reactor.

2. Experimental

2.1 Chemicals

Calcium sulfate dihydrate (>90%), magnesium sulfate heptahydrate (>98%), sodium hydrogenocarbonate (>99.5%) and sodium sulfate (>97%) were purchased from VWR International (Fontenay-sous-Bois, France). Sulfuric acid (95-97%) was obtained from Sigma Aldrich (Saint-Quentin-Fallavier, France). Sodium hydroxide (1 N) was provided by Honeywell Fluka (Seelze, Germany). Titanium (IV) oxysulfate-sulfuric acid (27-31%) solution for hydrogen peroxide (H_2O_2) detection was purchased from Sigma Aldrich (Saint-Quentin-Fallavier, France). These chemical reagents were used as purchased without further treatment.

2.2 Preparation of electrolyte

Electrolyte with and without carbonates contained sources of Ca^{2+} (150 mg L^{-1}) and Mg^{2+} (5 mg L^{-1}) dissolved in ultrapure water (18.2 MΩ cm) provided by PureLab ELGA Classic water purification system (Veolia Water, Antony, France). Electrolyte with carbonates contained a concentration of 60 mg-C L^{-1}. Initial values of pH and ionic conductivity were always adjusted to 7.6 and 1000 µS cm^{-1} respectively. A small quantity of sodium sulfate (1.4 to 5 mmol L^{-1}) was added when required in order to reach a constant ionic conductivity and strength (0.02 mol L^{-1}) for suitable comparison. The artificial WWTP effluent properties are representative to the average characteristics of effluent from the outlet of municipal WWTPs.

2.3 Electrochemical system

The effluent (0.5 L) to be treated was stored in a double-jacket stainless steel reservoir connected to a thermostatic bath in order to ensure a working temperature of 25°C (Bioblock Scientific, PolyScience, Niles, IL, USA). A peristaltic pump (Masterflex, Cole-Parmer, Vernon Hills, IL, USA) was used to circulate the solution. pH (Mettler Toledo InPro 4260i) and conductivity (Mettler Toledo InPro 7100i) were measured at regular time. The electrochemical cell was similar to the one described in previous work **[16]**. It consisted of a planar-electrodes filter-press type cell. Its body was made on-site and made of poly(methyl methacrylate) (PMMA). The material is chemically and thermally resistant in the applied operating conditions. Rubber seals were designed, built-in, to provide tightness and avoid leakage. Planar electrodes were used as anode and cathode. Double-sided boron-doped diamond (BDD) coated on Niobium (Nb) substrate (DiaCCon, Fürth, Germany) or Platinum plate (Ögussa, Vienna, Austria) with 50 cm^2 effective surface area each were used as anode. Stainless steel (Gantois Industries, Saint-Dié-des-Vosges, France) with the same effective surface area (50 cm^2) was used as cathode. Prior to utilization, stainless steel was preconditioned chemically by soaking it in sulfuric acid solution of 0.25 M. Non-conducting spacer made of polytetrafluoroethylene (PTFE) (Bohlender, Grünsfeld, Germany) was placed in-between to avoid contact between anode and

175 cathode. This spacer with micrometric thickness of 500 µm was used across this work, hence defining
176 inter-electrode distance of electrochemical cell. Electrolysis was carried out using a power supply
177 HMP4040 (Rohde & Schwarz, Meudon-la-Forêt, France). The influence of two sufficiently different
178 regions of current density were investigated in this work, i.e. 0.4 and 4 mA cm^{-2}. The latter was
179 selected because it has been defined as optimal current density from previous work where similar
180 reactor setting was used to degrade pharmaceutical pollutants **[16]**. All experiments were carried out
181 at least in duplicate to ensure reproducibility.

182 In preliminary experiments, two blank solutions were used. One composed of only sulfates (6.65
183 mmol L^{-1}) and another one containing carbonates at 60 mg-C L^{-1} with Na_2SO_4 (5 mmol L^{-1}) as
184 supporting electrolyte. Both blank electrolytes possessed similar initial pH value (7.6) and ionic
185 strength of 0.02 mol L^{-1}. Under another preliminary study where an absence of dissolved O_2 was
186 sought for the entire experiment, effluent in reservoir was bubbled with nitrogen gas (N_2) while it
187 was recirculating through the pilot initiating from 30 min before electrolysis until the end of
188 experiment. 500 µm inter-electrode distance and the highest current density condition (4 mA cm^{-2})
189 were implemented for preliminary experiments.

190 **2.4 Analytical methods**

191 Evolutions of Ca and Mg elements concentration were monitored, after filtering the samples using
192 Phenex 0.45 µm filter (Phenomenex, Le Pecq, France), via inductively coupled plasma optical
193 emission spectroscopy (ICP-OES) Thermo iCAP 6000 (Thermo Fisher, Illkirch-Graffenstaden,
194 France). The calibration was performed according to PlasmaCAL Custom Standard method (SCP
195 Sciences) using a certified multi-element solution (1000 mg L^{-1}, SCP Sciences, Villebon-sur-Yvette,
196 France). Ca and Mg elements measured by ICP-OES were assimilated to Ca^{2+} and Mg^{2+} when
197 dissolved in solution.

198 The concentration of sulfate (SO_4^{2-}) was measured using ionic chromatography Dionex ICS 6000
199 (Thermo Fisher, Noisy-Le-Grand, France). Its calibration curve was obtained from a series of
200 different known concentration of SO_4^{2-} prepared from a standard solution of 1000 µg mL^{-1}. The anion
201 exchange column IC Dionex^{TM} IonPac^{TM} AS18 (Thermo Fisher, Noisy-Le-Grand, France) equipped
202 with a column guard was used. The column was kept at 23°C. An aliquot of 15 µL of sample was
203 injected passing through the column. The temperature of samples tray was maintained at 20°C. The
204 ICS 6000 was equipped with a conductivity detector for detection system and it was kept constant at
205 35°C. The mobile phase rate was set at 1 mL min^{-1}.

206 Total inorganic carbon (TIC) was measured using a TOC-meter V_{CSH} TC/TN (Shimadzu, Marne-La-
207 Vallée, France). A TIC standard solution of 1000 µg mL^{-1} (TechLab, Metz, France) was used for
208 calibration and control.

209 Hydrogen peroxide (H_2O_2) concentration was measured via complexing H_2O_2-Ti^{4+} method [38]. UV-
210 2600 spectrophotometer (Shimadzu, Marne-La-Vallée, France) was used to detect maximum
211 absorbance of the complex at 410 nm wavelength. H_2O_2 concentration was deduced according to the
212 Beer-Lambert law from a calibration curve established with the use of standard H_2O_2 solutions.

213 Linear scan voltammetry (LSV), chrono-amperometry and chrono-potentiometry were performed
214 using a potentiostat (Ametek, Massy, France) connected to the designed electrochemical cell. The
215 electrode potential was reported against saturated silver chloride reference electrode (V/SSCE) in this
216 work.

217 **2.5 Recovery step of Ca and Mg elements**

218 The purpose of this step was to support the monitoring of the evolution of Ca and Mg concentrations
219 in the electrolyte using ICP-OES. It was assumed that if they decreased in solution over time, they
220 partook in deposition reactions and took solid form. The recovery of Ca and Mg from the solid form
221 could assert where the majority of the deposition reactions took place, if they occurred. The recovery

process was carried out using a solution of sulfuric acid at 0.25 M. The objective was to decrease the pH to re-dissolve the deposits into ionic form. Once completely dissolved, the acid solution was filtered through Phenex 0.45 µm filter (Phenomenex, Le Pecq, France) and was analyzed by ICP-OES to determine the Ca and Mg concentrations. To ensure a thorough recovery of cations that might undergo scaling in different compartment of experimental pilot, the recovery step was performed on cathode, anode as well as pilot tubing. Hence, knowing the initial and final concentration of cations in the electrolyte, mass balance of cations could be performed to observe the distribution of deposition formed in and out of the electrochemical reactor in addition to attesting a quasi-complete recovery of cations.

Theorem of conservation of mass tells that the sum of mass *i* element (Ca and Mg) recovered at different compartment of experimental pilot at the end of experiment should be equal to the initial mass of *i* present in electrolyte before the electrolysis, if there is no loss in the closed system. Mass balance and percentage recovery of *i* are then defined in **Eq. (8)** and **Eq. (9)**, respectively:

$$m_{recovered} = m_{f,elec} + m_{anode} + m_{cathode} + m_{tube} \quad (8)$$

$$\left(m_{recovered} \,/\, m_{i,elec}\right) \times 100 = \%\, recovery \quad (9)$$

where $m_{recovered}$ is the total mass (in mg) of *i* recovered from different compartment, $m_{i,elec}$ the initial mass of *i* element in electrolyte before electrolysis, $m_{f,elec}$ the mass of *i* that remains in electrolyte at the end of electrolysis, m_{anode} the mass of *i* recovered from the surface of anode, $m_{cathode}$ the mass of *i* recovered from the surface of cathode and m_{tube} the mass of *i* recovered from the surface of tubing of pilot.

3. Modelling

3.1 Electrolyte containing Mg^{2+} and Ca^{2+}

Mg^{2+} and Ca^{2+} react with OH^- to produce precipitates of $Mg(OH)_2$ and $Ca(OH)_2$ when the product of concentrations of both cations with OH^- exceeds the constants of solubility of $Mg(OH)_2$ ($K_{S,Mg(OH)_2}$) ($K_{S,Mg(OH)_2} = 5.61 \times 10^{-12}$ **[39, 40]**) and of $Ca(OH)_2$ ($K_{S,Ca(OH)_2}$) ($K_{S,Ca(OH)_2} = 5.00 \times 10^{-6}$ **[39, 40]**) respectively. Knowing Mg^{2+} and Ca^{2+} concentrations in the system, the concentration of OH^- at which its product reaches the $K_{S,Mg(OH)_2}$ and $K_{S,Ca(OH)_2}$ values, respectively, can be calculated. It is noted as critical OH^- concentration (OH^-_{crit}).

During the electrolysis, OH^- ions are produced on cathode by reduction of either dissolved O_2 via 4-electrons reaction (**Eq. (1)**) and/or water via 2-electrons reaction (**Eq. (2)**). Since both reactions took place in parallel on cathode in our system under the applied current densities, they have been considered as competing reactions. CE_{O_2} and CE_{H_2O} terms were used to proportionate the current efficiency as a result of the reduction of O_2 and H_2O respectively. The rate of production of OH^- (r_{OH^-}) on cathode in batch mode can thus be written as in **Eq. (10)**:

$$r_{OH^-} = + \frac{d[OH^-]}{dt} = \frac{\nu_{O_2}\, j_{app}}{n_{O_2}\, F} CE_{O_2} + \frac{\alpha\, \nu_{H_2O}\, j_{app}}{n_{H_2O}\, F} CE_{H_2O} \quad (10)$$

where ν_{O_2} and ν_{H_2O} are the stoichiometry coefficient of OH^- via reaction of reduction of O_2 (**Eq. (1)**) and H_2O (**Eq. (2)**) respectively, while n_{O_2} and n_{H_2O} are their number of electrons involved in those faradaic reactions, j_{app} is the applied current density in mA cm^{-2} and F is the Faraday constant (96,485 C mol^{-1}). α is a corrective term (α < 1) assigned to the faradaic production of OH^- which occurs concomitantly with physical evolution of gas bubbles on cathode surface at high applied current density. In accordance to **Eq. (2)**, H_2 gas also evolves when H_2O is reduced to OH^-. H_2 gas evolution is more intense when higher current density value is used, according to the Faraday's law. Gas evolution on cathode surface contributes to two major consequences; firstly, less surface area could be available for mineral deposition on cathode surface **[41]**. Secondly, it could promote detachment of deposits occurring on the electrode **[42, 43]**.

On the surface of cathode, OH^- ions are produced abundantly and continuously. Water is the solvent of electrolyte thus its electrochemical reduction is limitless. Meanwhile, dissolved O_2 are not only consumed on cathode (**Eq. (1)**), but it is also concomitantly produced on anode through water oxidation (**Eq. (11)**).

$$2H_2O \rightarrow O_2 + 4H^+ + 4e^- \quad (11)$$

In microfluidic configuration, the distance between cathode and anode is very small thus the replenishment of dissolved O_2 could take place continuously **[44]**. As a result, once OH^-_{crit} is reached, OH^- concentration is considered constant and it does not vary whilst reacting with Mg^{2+} and Ca^{2+} because the concentration of OH^- is significantly larger and in excess compared to the cations concentrations. In addition, it is assumed that Mg^{2+} and Ca^{2+} were not reduced or oxidized by direct electrochemical reduction or oxidation, so that their oxidation state remained constant all along the electrolysis **[45]**.

Hence, according to **Eqs. (3)-(4)**, the rate of reaction of Mg^{2+} and Ca^{2+} can be written according to **Eq. (12)** and **Eq. (13)** respectively:

$$r_{Mg^{2+}} = -r_{Mg(OH)_2} = -k_{Mg(OH)_2}[Mg^{2+}][OH^-]^2 \quad (12)$$

$$r_{Ca^{2+}} = -r_{Ca(OH)_2} = -k_{Ca(OH)_2}[Ca^{2+}][OH^-]^2 \quad (13)$$

where $k_{Mg(OH)_2}$ and $k_{Ca(OH)_2}$ are the third order rate constants regarding the reaction of precipitation of $Mg(OH)_2$ and $Ca(OH)_2$ respectively in $L^2\ mol^{-2}\ s^{-1}$, while $[Mg^{2+}]$, $[Ca^{2+}]$ and $[OH^-]$ are the molar concentration (in mol L^{-1}) of Mg^{2+}, Ca^{2+} and OH^- ions, respectively.

3.2 Electrolyte containing Ca^{2+} and CO_3^{2-}

Ca^{2+} reacts with CO_3^{2-} to form $CaCO_3$ precipitates when the product of concentrations of both ions exceeds the constant of solubility of $CaCO_3$ ($K_{S,CaCO_3}$) ($K_{S,CaCO_3}$ = 3.36 × 10^{-9} **[40, 46-48]**).

Supersaturation degree (S) of $CaCO_3$ is defined in **Eq. (14)** and follows by its supersaturation index in **Eq. (15) [49, 50]**.

$$S = \frac{[Ca^{2+}]\,[CO_3^{2-}]}{K_{sp,CaCO_3}} \quad (14)$$

$$SI = log_{10}(S) \quad (15)$$

Thermodynamically, $CaCO_3$ can precipitate when S > 1 (or SI > 0). Carbonates concentration can be estimated from TIC measurement that corresponds to the sum of all forms of inorganic carbon (**Eq. (16)**):

$$\text{TIC} = [H_2CO_3] + [HCO_3^-] + [CO_3^{2-}] \quad (16)$$

where H_2CO_3 is carbonic acid and HCO_3^- is bicarbonate ion.

The inorganic carbon species are linked together by acidity constants K_{a1} and K_{a2} given in **Eqs. (17)–(18)**, respectively.

$$K_{a1} = \frac{[H^+]\,[HCO_3^-]}{[H_2CO_3]} \quad (17)$$

$$K_{a2} = \frac{[H^+]\,[CO_3^{2-}]}{[HCO_3^-]} \quad (18)$$

Their ratios are therefore governed by the solution pH. pK_{a1} and pK_{a2} values are 6.3 and 10.4 **[51]**, respectively. Under the range of our pH operating conditions and at the proximity of cathode surface, the quantity of H_2CO_3 is negligible and the expression of TIC can be simplified into **Eq. (19)**.

$$\text{TIC} = [HCO_3^-] + [CO_3^{2-}] \quad (19)$$

CO_3^{2-} concentration is related to the concentration of OH^- produced on cathode surface by its equilibrium with HCO_3^- in agreement with **Eq. (5)** and **Eq. (18)**. Hence, the evolution of interfacial

CO_3^{2-} concentration ($[CO_3^{2-}]_{int,t}$) can be estimated from TIC values by combining **Eqs. (10)**, **(18)** and **(19)** giving out an expression in **Eq. (20)**.

$$[CO_3^{2-}]_{int,t} = \frac{K_{a2} \times TIC_t}{\frac{K_W}{[OH^-]_t} + K_{a2}} \quad (20)$$

where K_{a2} and the concentration of interfacial CO_3^{2-}, OH^- and TIC are expressed in mol L^{-1} while the equilibrium constant of auto-ionization of water (K_W) is considered equaled to 10^{-14} at 25°C.

According to **Eq. (6)**, the rate of reaction of Ca^{2+} and CO_3^{2-} producing $CaCO_3$ can be defined as indicated in **Eq. (21)**:

$$r_{Ca^{2+}} = r_{CO_3^{2-}} = -r_{CaCO_3} = -k_{CaCO_3}[Ca^{2+}][CO_3^{2-}]_{int} \quad (21)$$

where k_{CaCO_3} is the second order rate constant (in L mol^{-1} s^{-1}) regarding the reaction of precipitation of $CaCO_3$. Identically to the Mg^{2+}/Ca^{2+} system (section **3.1**), OH^- accumulates at the vicinity of cathode during the electrolysis.

3.3 Electrolyte containing Mg^{2+} and CO_3^{2-}

In absence of Ca^{2+}, Mg^{2+} can precipitate in the form of $Mg(OH)_2$ upon reaching OH_{crit}^- as well as $MgCO_3$ when the product of concentrations of Mg^{2+} and CO_3^{2-} exceeds thermodynamic solubility constant of $MgCO_3$ ($K_{S,MgCO_3}$) ($K_{S,MgCO_3} = 1.59 \times 10^{-8}$ **[52]**). Local alkalization remains valid at the surface of cathode. Knowing the fact that Mg^{2+} could participate in the precipitation reactions of $Mg(OH)_2$ and $MgCO_3$, on top of kinetic law defined in **Eq. (12)**, the rate of reaction of Mg^{2+} can be rewritten in **Eq. (22)** as follow:

$$r_{Mg^{2+}} = -r_{Mg(OH)_2} - r_{MgCO_3} = -k_{Mg(OH)_2}[Mg^{2+}][OH^-]^2 - k_{MgCO_3}[Mg^{2+}][CO_3^{2-}] \quad (22)$$

where k_{MgCO_3} is the second order rate constant (in L mol^{-1} s^{-1}) regarding the reaction of precipitation of $MgCO_3$.

3.4 Electrolyte containing Mg^{2+}, Ca^{2+} and CO_3^{2-}

In the matrix of electrolyte containing Mg^{2+}, Ca^{2+} and CO_3^{2-}, both Mg^{2+} and Ca^{2+} can undergo precipitation in accordance to **Eqs. (3)-(4)** and **Eqs. (6)-(7)**. The phenomenon of local alkalization remains accurate in this system.

In the presence of Mg^{2+}, depositing $MgOH_2$ consumes OH^- over time. The cathodic production of OH^- in **Eq. (10)** is modified taking into account this event as indicated in **Eq. (23)**:

$$r_{OH^-} = + \frac{d[OH^-]}{dt} = \frac{\nu_{O_2}\, j_{app}}{n_{O_2}\, F} CE_{O_2} + \frac{\alpha\, \nu_{H_2O}\, j_{app}}{n_{H_2O}\, F} CE_{H_2O} - 2\, k_{Mg(OH)_2}[Mg^{2+}][OH^-]^2 \quad (23)$$

3.5. Modelling software and fitting evaluation

Aquasim **[53]** was used to model the evolution of Mg^{2+}, Ca^{2+} and CO_3^{2-}. The fitting between experimental data and theoretical model was evaluated using root mean square error (RMSE), model efficiency (ME) and index of agreement (IOA) according to **Eq. (24)**, **Eq. (25)** and **Eq. (26)**, respectively **[54]**:

$$RMSE = \sqrt{\frac{\sum_{i=1}^{K}(y_i - y_i')^2}{K}} \quad (24)$$

$$ME = 1 - \frac{\sum_{i=1}^{K}(y_i - y_i')^2}{\sum_{i=1}^{K}(y_i - y_M)^2} \quad (25)$$

$$IOA = 1 - \frac{\sum_{i=1}^{K}(y_i - y_i')^2}{\sum_{i=1}^{K}(|y_i' - y_M| + |y_i - y_M|)^2} \quad (26)$$

where K is the number of steps of checked values, y_i' is the experimental value, y_i is the corresponding simulated value and y_M is the average of simulated value.

4. Results and discussion

4.1 Stability of anions in blank solutions using BDD or Pt anode

Preliminary experiments were conducted in the microfluidic reactor to check on the behavior of anions (SO_4^{2-} and HCO_3^-/CO_3^{2-}) during electro-oxidation in the absence of depositing elements. BDD and Pt anodes were used to verify the involvement of $^{\bullet}OH$ towards any oxidation of anions. The former is well-known for its high overpotential for oxygen evolution reaction (OER). Consequently, physi-sorbed $^{\bullet}OH$ are produced at anode vicinity **[55, 56]**. Contrastingly, the overpotential for OER with Pt anode is low. Thus $^{\bullet}OH$ is chemi-sorbed on the anode surface, making the radical not available **[57]**.

The evolution of concentration of SO_4^{2-} and TIC are depicted in **Fig. 1**. It has been noticed that the concentration of both anions remained constant throughout the entire electro-oxidation experiments whether BDD or Pt was used as anode. First deduction that can be made is that SO_4^{2-} and HCO_3^-/CO_3^{2-} anions were stable during the electro-oxidation process whatever the anode employed. It means that they will not interfere if there is occurrence of electro-precipitation on cathode surface. Secondly, under these applied conditions, the formation of oxidizing agent of $^{\bullet}OH$ did not inflict towards the degradation of SO_4^{2-} and HCO_3^-/CO_3^{2-} anions. Anode potential was measured to be +2.40 V/SSCE (or +2.60 V/SHE), which already hit the standard potential of formation of $^{\bullet}OH$ when 4 mA cm^{-2} is applied. The oxidation conditions were not strong enough to oxidize SO_4^{2-} into peroxydisulfates ($S_2O_8^{2-}$) **[58]** and CO_3^{2-} into peroxydicarbonates ($C_2O_6^{2-}$) **[59, 60]** with $SO_4^{\bullet-}$ and $CO_3^{\bullet-}$ as intermediates, respectively. Moreover, anion of strong acid such as SO_4^{2-} is very unlikely to form complex with alkaline-earth cations such as Ca^{2+} and Mg^{2+} **[61]**. In overall, $^{\bullet}OH$ involvement in microfluidic reactor set-up did not lead to the oxidation of SO_4^{2-} and HCO_3^-/CO_3^{2-} anions in blank electrolytes during electro-oxidation experiments. In overall, the presence of $^{\bullet}OH$ in our applied microfluidic reactor conditions could thus be omitted from the developed theoretical models and was confirmed further in the next sections.

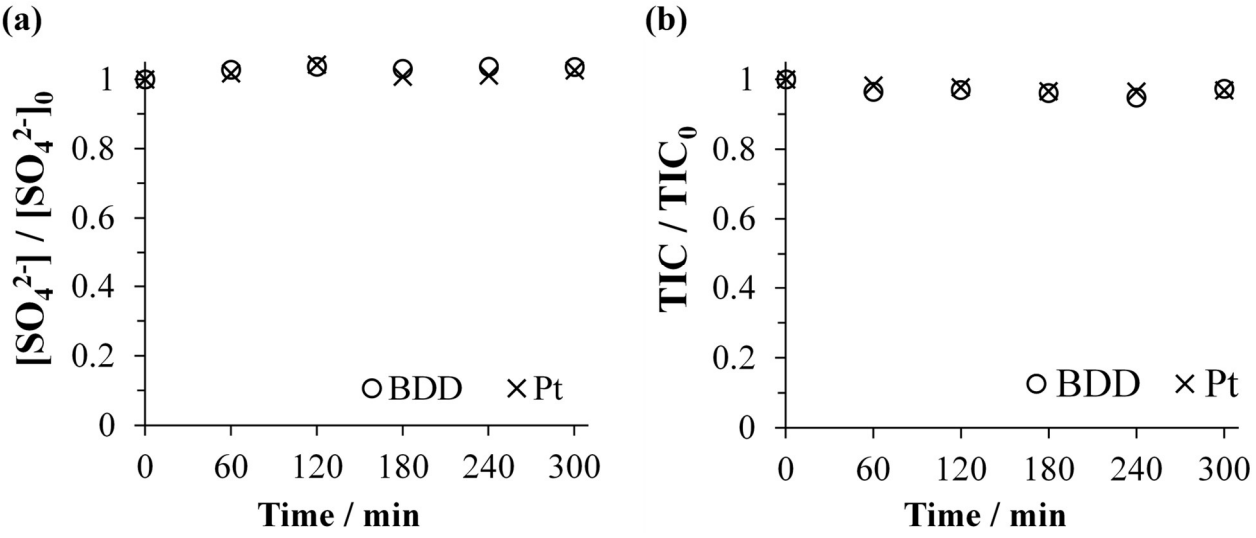

371

372 **Fig. 1**. Evolution of concentration of **(a)** SO_4^{2-} (in blank solution containing sulfates only) and **(b)**
373 TIC (in blank solution containing carbonates only) during the electrolysis of blank solutions using
374 BDD (○) or Pt (×) as anode. Cathode: stainless steel, ionic strength of both blank solutions: 0.02
375 mol L^{-1}, applied current density: 4 mA cm^{-2} and inter-electrode distance: 500 µm.

376 **4.2 Local alkalization on cathode surface: reactions' selectivity between reduction of dissolved**
377 **O_2 and water**

378 According to **Eq. (1)** and **Eq. (2)** respectively, both dissolved O_2 and H_2O can undergo faradaic
379 reduction generating OH^- (**Eq. (10)**). To identify the weight of contribution of dissolved O_2 to produce
380 OH^- with respect to local alkalization phenomenon, tests in presence and absence of dissolved O_2
381 were conducted. Under the investigated micrometric distance, anodic activity might be involved in
382 this selectivity, since H_2O could be also oxidized to O_2.

383 **Fig. 2** plots the evolution of concentration of Mg^{2+}, Ca^{2+} and TIC in the experiments with and without
384 dissolved O_2. In both cases, the concentration of all species decreased regardless of presence of
385 dissolved O_2. This indicates that the initial presence of dissolved O_2 was insignificant towards the
386 phenomenon of local alkalization, and consequently towards the formation of deposits on cathode
387 surface. Notably from **Fig. 2(a)** and **Fig. 2(b)**, it has been deduced that the source of OH^- ions came
388 mainly from reduction of water and not from dissolved O_2. A slight decrease in the electro-

389 precipitation of Ca^{2+} in absence of dissolved O_2 was due to slightly lesser amount of OH^- participating
390 in thermodynamic shift of HCO_3^-/CO_3^{2-} towards the formation of CO_3^{2-} (**Fig. 2(b)**). Thus, lesser
391 extent of $CaCO_3$ electro-precipitation was observed.

392 Under theses setups, the concentration of electrogenerated H_2O_2 was measured to further study the
393 contribution of dissolved O_2 reduction producing OH^- ions in accordance with **Eq. (27)**.

394 $$O_2 + 2H_2O + 2e^- \leftrightarrow H_2O_2 + 2OH^- \quad (27)$$

395 The H_2O_2 production was found to be very small (maximum concentration went up to 1.8 µmol L^{-1},
396 data not shown), whatever the applied current density. Most of H_2O_2 concentration values fell below
397 the limit of quantification of the method, determined to be 0.8 µmol L^{-1}. This observation was
398 attributed to the low H_2 evolution overvoltage on stainless steel cathode **[62]**. Similar poor production
399 of H_2O_2 on stainless steel cathode was reported by Sopaj et al. **[38]**. They measured approximately
400 40 µmol L^{-1} of H_2O_2 under their experimental setup when 4.8 mA cm^{-2} was applied **[38]**. Unlike the
401 configuration presented in our work, compressed air was continuously bubbled under their
402 experimental setup to supply dissolved O_2 to promote the Fenton reaction, which explains the
403 difference in measured H_2O_2 concentration.

404 CE_{O_2} and CE_{H_2O} in **Eq. (10)** and **Eq. (23)** were estimated via **Eqs. (28)-(29)** at each value of current
405 density investigated in this work. Their values are tabulated in **Table 1**. The calculations are attached
406 as **Text S1** in supplementary materials.

407 $$CE_{O_2} = \frac{n_{e^-} F N_{O_2}}{J_{app} t} \quad (28)$$

408 $$CE_{H_2O} = 1 - CE_{O_2} \quad (29)$$

409 where n_{e^-} is the number of electron exchanged in **Eq. (27)**, N_{O_2} is the quantity of dissolved O_2 (in
410 mol) reduced to H_2O_2 in **Eq. (27)**, J_{app} is the applied current (in A) and t is the electrolysis time.

411 **Table 1.** Estimation of CE_{O_2} and CE_{H_2O} in faradaic production of OH^- on cathode.

j_{app} / mA cm^{-2}	N_{O_2} / µmol	CE_{O_2} / %	CE_{H_2O} / %
0.4	0.6	0.16	99.84
4	0.9	0.02	99.98

412 To conclude, local alkalization on cathode surface principally occurred due to the reduction of H_2O
413 with only slight involvement of dissolved O_2 under our experimental setup. The latter was
414 electrocatalytically reduced to OH^- with negligible production of H_2O_2 on stainless steel. Our
415 proposed model takes into consideration this observed selectivity given by higher faradaic yield of
416 CE_{H_2O} in producing OH^- as deduced in **Table 1** when applied to **Eq. (10)** and **Eq. (23)**.

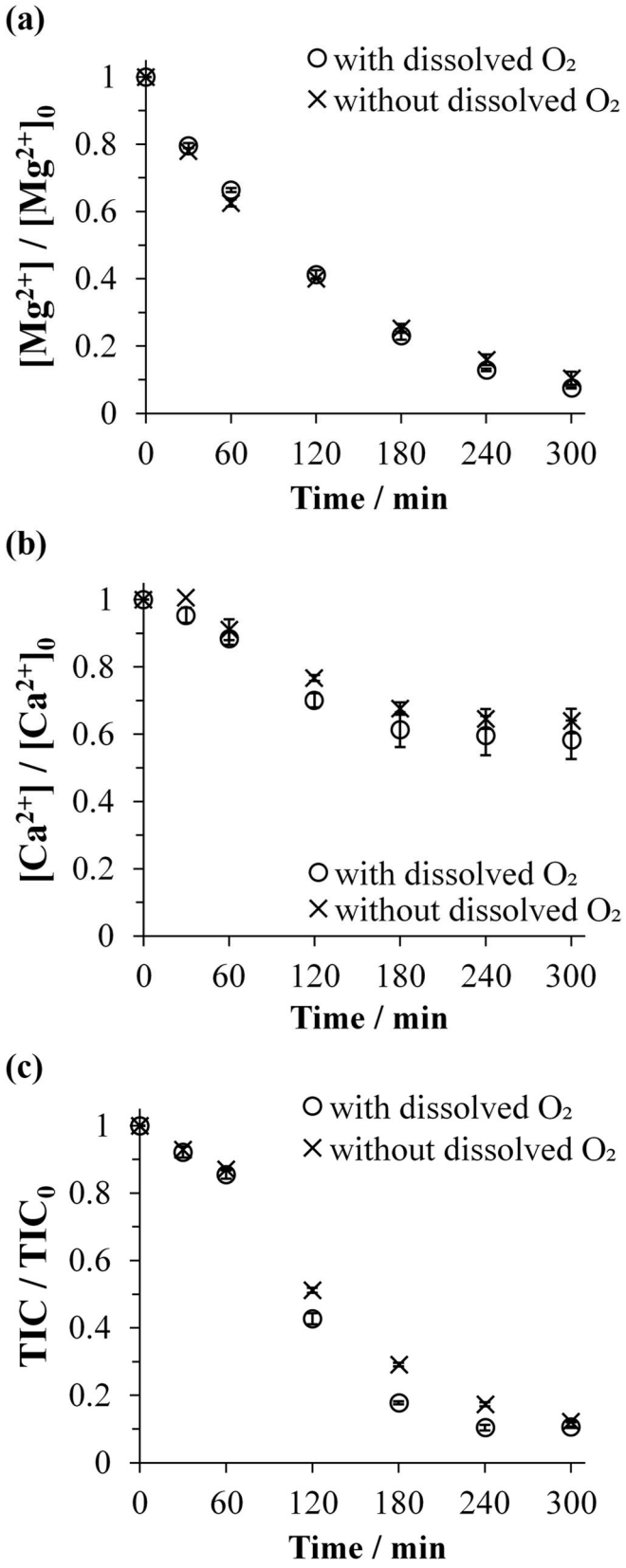

417

418 **Fig. 2**. Evolution of concentration of **(a)** Mg^{2+}, **(b)** Ca^{2+} and **(c)** TIC during the electrolysis of

419 artificial effluent containing 150 mg L^{-1} of Ca^{2+}, 5 mg L^{-1} of Mg^{2+} and 60 mg-C L^{-1} of HCO_3^-/CO_3^{2-}

420 in absence (×) (via bubbling with N_2 gas) and presence (○) of dissolved O_2 throughout the

experiment. Anode: BDD, cathode: stainless steel, applied current density: 4 mA cm^{-2} and inter-electrode distance: 500 µm.

4.3 Influence of electromigration of ionic species

Although calcium and magnesium deposits are formed on the surface of cathode during electrolysis, Ca^{2+} and Mg^{2+} do not participate in direct electron transfer to yield Ca metal (Ca(s)) and Mg metal (Mg(s)) respectively. The reduction of Ca^{2+} and Mg^{2+} each by two electrons need to overcome a strong thermodynamic barrier ($E^0_{Ca^{2+}/Ca_{(s)}}$ = -2.84 V/SHE and $E^0_{Mg^{2+}/Mg_{(s)}}$ = -2.356 V/SHE **[63]**), and these strong reduction conditions are not involved in the present study (cathode potential determined to be -1.34 V/SHE). Instead, they reacted chemically with respective counter-ions on the surface of cathode, producing scaling when solubility constant of precipitates was achieved. Despite not being electroactive elements in regard to driving force of potential difference across electrochemical reactor, Ca^{2+} and Mg^{2+} mobility towards cathode surface might be involved in the displacement of ionic species jointly present in the bulk. In agreement with the Nernst-Planck equation, Ca^{2+} and Mg^{2+} were transported by forced convection thanks to electrolyte flow in-between electrodes. Under stationary conditions, they underwent diffusion from electrolyte bulk through finite boundary layer (i.e. diffusion layer), towards reactive zone at the proximity of cathode surface. Then through migration, they were mobilized to fulfill electro-neutrality on cathode surface as the consequence of local alkalization **[64-66]**. The two current densities investigated in this study were both above the initial limiting current density (determined to be 0.25 mA cm^{-2} using j_{lim} calculation **[67, 68]** (**Text S2**), which was then confirmed with limiting current density plateau on linear scan voltammogram (**Fig. S1**)) for aforementioned electrochemical cell setup while producing OH^-. Hence, electrochemical reactions taking place on the surface of cathode were considered limited by the mass transport.

Therefore, in this section, under constant hydrodynamic parameters, the influence of electromigration of ionic species was investigated by varying the ionic strength of artificial effluent using Na_2SO_4 as supporting electrolyte. **Table 2** summarizes the values of ionic transference number for the different cases. They were calculated using **Eqs. (30)-(31) [69]** under the assumption that our electrolytic system complied with the restriction of infinite dilution where interaction between ions was not occurring.

$$t_i = \frac{z_i\, C_i\, u_i}{\sum_i z_i\, C_i\, u_i} \tag{30}$$

with

$$u_i = \frac{\lambda_i}{z_i\, F} \tag{31}$$

where t_i is the transference number, z_i the ionic charges, u_i the ionic mobility (in $m^2\ s^{-1}\ V^{-1}$), C_i the molar concentrations of ionic species (in mol L^{-1}) and λ_i the ionic molar conductivity (in S m^2 mol^{-1}).

Table 2. Ionic transference number for artificial effluent containing 150 mg L^{-1} of Ca^{2+}, 5 mg L^{-1} of Mg^{2+} and 60 mg-C L^{-1} of TIC without and with addition of Na_2SO_4 at different concentrations.

Ionic strength / mol L^{-1}	**Ionic transference number**				
	Ca^{2+}	Mg^{2+}	Na^{+}	HCO_3^-	SO_4^{2-}
0.02 (without Na_2SO_4)	0.218	0.011	0.123	0.339	0.309
0.04	0.120	0.006	0.241	0.187	0.447
0.10	0.050	0.002	0.325	0.077	0.545

As can be seen from **Table 2**, the more Na_2SO_4 was added to increase the ionic strength of artificial effluent, the more ionic mobility of Ca^{2+}, Mg^{2+} and HCO_3^-/ CO_3^{2-} were minimized by increasing transport activity of Na^{2+} and SO_4^{2-}.

Fig. 3 depicts the trend of evolution of concentration of Mg^{2+}, Ca^{2+} and TIC when the investigated artificial effluent had different ionic strengths. The concentration of each ion decreased over time regardless of value of ionic strength. It seemed to have very little impact on the variation of the concentration of Ca^{2+} and TIC as previously suggested by Tlili et al., where migration might play some role with respect to only more concentrated species in the system **[64]**. Standard deviations were calculated between results obtained with the electrolytes with enhanced ionic mobility in comparison to the one without supporting electrolyte. The average values are listed in **Table S1**. The two highest deviation were obtained in Mg^{2+} and TIC concentration with evaluated deviation as low as 0.049 and 0.042, respectively. Therefore, the ionic strength of electrolyte had minor effect within the range of studied electrolyte concentrations towards the occurring mineral deposition on cathode surface. Electromigration of ionic species other than Ca^{2+}, Mg^{2+} and HCO_3^-/CO_3^{2-} did not influence the mobility of the precipitating elements in-between electrodes inside microfluidic electrochemical reactor. Mass transport by diffusion was then the rate-limiting factor. Based on these results, the effect of electromigration could be omitted from the theoretical model proposed in section **3**. The addition of small quantity of supporting electrolyte (from 1.4 to 5 mmol L^{-1}) to achieve constant ionic strength across different investigated matrices of electrolyte will not influence the kinetics of mineral electro-precipitation in experimental results presented onwards.

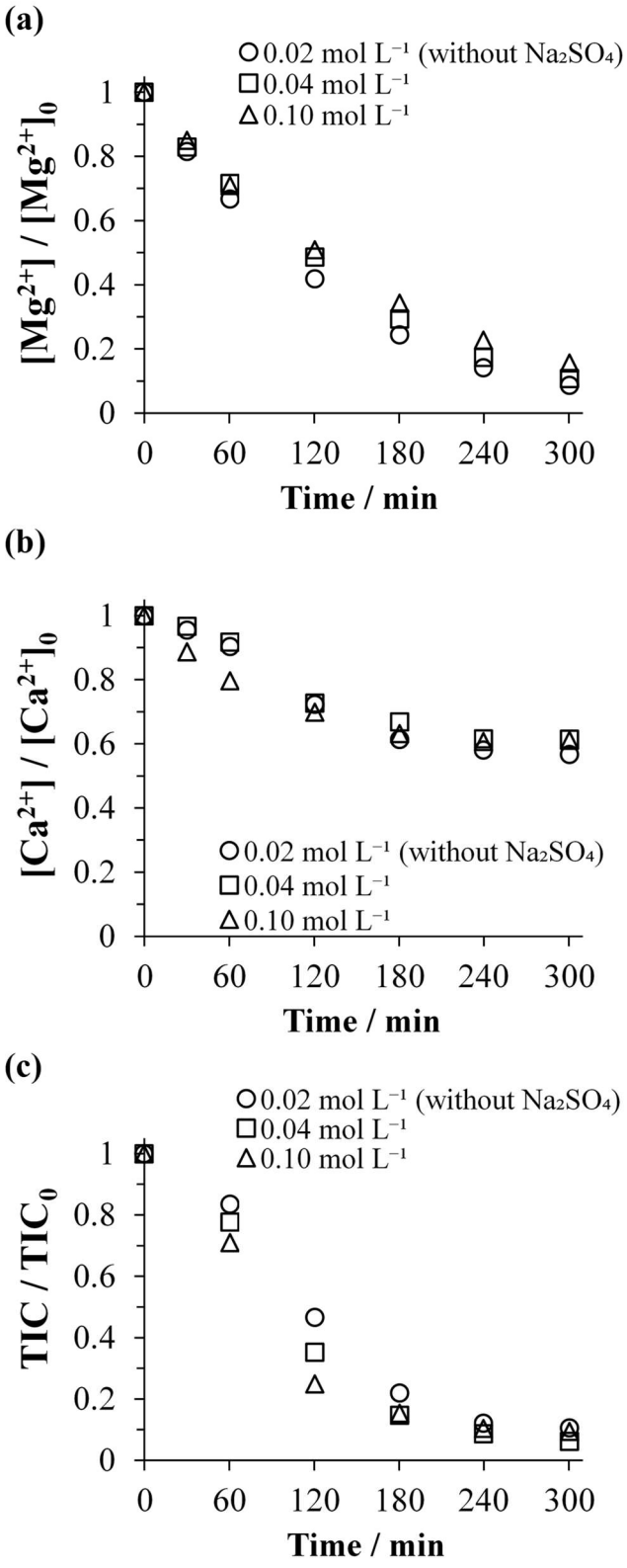

478

479 **Fig. 3**. Evolution of concentration of **(a)** Mg^{2+}, **(b)** Ca^{2+} and **(c)** TIC during the electrolysis of

480 artificial effluents bearing different ionic strengths of 0.02 (○) (without the addition of supporting

481 electrolyte), 0.04 (□) and 0.10 (△) mol L^{-1}. Anode: BDD, cathode: stainless steel, applied current

482 density: 4 mA cm^{-2} and inter-electrode distance: 500 µm.

4.4 Influence of matrix of electrolyte

4.4.1 Influence of CO_3^{2-} towards the mineral electro-precipitation

Electrolysis of electrolyte containing Mg^{2+} and Ca^{2+}, in presence and absence of CO_3^{2-}, in the microfluidic flow-by reactor were carried out by applying 0.4 and 4 mA cm^{-2} and the results are plotted in **Fig. 4** and **Fig. 5**. From **Fig. 4**, it could firstly be observed that Ca^{2+} did not precipitate in the electrolyte without carbonate at both current densities. It precipitated only in presence of carbonate. Thus, it has been concluded that $Ca(OH)_2$ was not produced throughout these series of experiment and Ca^{2+} only electro-precipitated to form $CaCO_3$. This observation can be supported by the value of thermodynamic constant of solubility of $Ca(OH)_2$ that is high (5.00×10^{-6} **[39, 40]**) - thus highly soluble -, hence the interfacial pH never reached the OH^-_{crit} (i.e. 36.6 mol m^{-3}, pH = 12.6) to precipitate with Ca^{2+}. Secondly, according to **Fig. 5**, Mg^{2+} only precipitated at 4 mA cm^{-2} and no Mg^{2+}-based deposition occurred at 0.4 mA cm^{-2}. At low current density, since no decrease of Mg^{2+} was observed, it can be concluded that $Mg(OH)_2$ was not electro-precipitated. Same remark was given by Deslouis et al. **[30]** where they did not observe precipitation of $Mg(OH)_2$ when interfacial pH of 9.3 was not yet reached. Our result tells that there was a plateau at 4 mA cm^{-2} at the very beginning of electrolysis up to 7 min before Mg^{2+} started to deposit forming $Mg(OH)_2$, as soon as OH^-_{crit} (0.16 mol m^{-3}, interfacial pH = 10.2) was reached (**Fig. 5**). Then, during the first hour of electrolysis at 4 mA cm^{-2}, a slightly higher kinetics of $Mg(OH)_2$ deposition was observed in the electrolyte without carbonate. In the presence of CO_3^{2-}, there was perhaps a weak competition between $Mg(OH)_2$ and $CaCO_3$ for active site on the surface of cathode **[36, 70]**. However, it was not accounted for $MgCO_3$, otherwise the kinetics of precipitation with the electrolyte containing CO_3^{2-} would be faster and not slower than the one without CO_3^{2-}. To conclude, Mg^{2+} electro-precipitated independently with regard to carbonate ions.

Moreover, it can be seen in **Fig. 4** that $CaCO_3$ was already deposited at low current density, unlike $Mg(OH)_2$ even though the thermodynamic constant of solubility of $Mg(OH)_2$ is lower than that of

508 $CaCO_3$. Similar observation was reported by Okstad et al. [71]. The higher initial concentration of
509 Ca^{2+} - implemented to simulate the composition of reclaimed wastewater from urban WWTPs - can
510 be one of the reasons of this observation, whereby supersaturation degree was already high. On top
511 of that, experimental results showed that 7.2% more $CaCO_3$ deposition occurred at 0.4 mA cm^{-2} in
512 comparison to higher applied current density of 4 mA cm^{-2}. To our understanding, once $CaCO_3$
513 electro-precipitation started to occur, it took place regardless of applied current density as long as the
514 current density was equal or higher than the starting point of the nucleation of $CaCO_3$ crystal. In case
515 of low and high applied current densities investigated in this work, $CaCO_3$ already formed at the low
516 current density (0.4 mA cm^{-2}). It would behave similarly at higher applied current density except that
517 within the latter, oxidation and reduction of solvent on the surface of electrodes were occurring at
518 higher rates leading to higher amount of electro-generated gas. Given the fact that at 0.4 mA cm^{-2} it
519 was already exceeding the limiting current density (0.25 mA cm^{-2}, see section **4.3**), gas production
520 was therefore occurring at both applied conditions. It means that the influence of gas evolution was
521 taking place concomitantly with the electro-precipitation on cathode surface [72], but in an antagonist
522 way according to the level of gas production. At 0.4 mA cm^{-2}, the lower evolution of gas on the
523 surface of electrode could enhance the mass transfer of reactive towards the electrodes [73-76]. This
524 enhancement would be attributed to firstly micro-convection, even at small value of current density
525 [73], due to evolving and departing gas bubbles from the electrode surface. Secondly, forced
526 convection or macro-convection owing to movement and displacement of bubbles over the electrode
527 surface could also occur [74-76]. Therefore, transport of Ca^{2+} and Mg^{2+} towards cathode surface for
528 precipitation reaction were enhanced at the low current density condition. This could explain why
529 slightly more $CaCO_3$ was obtained at lower current density. Contrastingly, higher intensity of gas
530 evolution is expected over the surface of cathode at high applied current density (4 mA cm^{-2}).
531 Therefore, bubble coverage at the electrode surface should have increased as described by Vogt et al.
532 [41]. Therefore, the more intense gas evolution at higher applied current density could have disturbed

533 the layer of $CaCO_3$ nuclei and in-parallel promoted the detachment of $CaCO_3$ deposit **[42, 43, 62]**.
534 Consequently, less electro-precipitation of $CaCO_3$ was observed at higher applied current density.

535 Furthermore, in presence of Ca^{2+} (150 mg L^{-1}) and carbonates (TIC of 60 mg-C L^{-1}), supersaturation
536 index (SI) defined in **Eq. (15)** equaled to 0.89 in the initial electrolyte. It means that Ca^{2+} and CO_3^{2-}
537 concentrations in the bulk were already above their equilibrium state in water (where SI = 0) initially
538 **[49]**. From the thermodynamic point of view, $CaCO_3$ precipitation in the bulk and scaling on metal
539 substrate could occur. However, the induction time for homogenous and heterogeneous $CaCO_3$
540 nucleation varies in function of physico-chemical component of bulk liquid as well as metal substrate
541 **[29, 50, 77]**. According to Gabrielli et al., thermodynamics requires a 40-fold supersaturation before
542 the precipitation in the bulk can be observed, i.e. equivalent to SI value around 1.6 **[18, 77, 78]**. It has
543 also been demonstrated that under low supersaturation conditions, very long induction time (12 h)
544 was required before observing scaling on metal substrate **[79]**. This might be one of the reasons
545 sluggish kinetics of electro-precipitation of $CaCO_3$ was observed at the very beginning of electrolysis
546 in **Fig. 4**. With respect to the evolution of experimental TIC concentrations (**Fig. S2 (a-d)**) as well as
547 to the modeled interfacial CO_3^{2-} concentrations illustrated in **Fig. 6**, this slow initial kinetics were
548 also noticed. From **Fig. 6**, it can be noticed that on cathode surface, CO_3^{2-} departed from its initial
549 bulk concentration and rapidly increased owing to electrogenerated OH^- once the electrolysis started.
550 With increasing quantity of interfacial CO_3^{2-}, more CO_3^{2-} was readily available to react with Ca^{2+} to
551 form $CaCO_3$ scaling. The supersaturation degree quickly increased, thus promoting the deposition of
552 $CaCO_3$. The concentration of interfacial CO_3^{2-} kept increasing as long as the rate of production of
553 OH^- was superior to the rate of production of $CaCO_3$ (or CO_3^{2-} consumption at the interface). During
554 this period, more CO_3^{2-} was shifted from HCO_3^- form since the OH^- concentration also increased, the
555 phenomenon that contributed towards local alkalization. A peak was attained when the rate of OH^-
556 production equaled that of CO_3^{2-} consumed. Beyond this peak, the rate of electro-precipitation of
557 $CaCO_3$ declined due to decreasing concentration of both Ca^{2+} and CO_3^{2-} in the electrolyte at later
558 stage of electrolysis as can be observed in **Fig. 4**. When comparing the evolution of interfacial CO_3^{2-}

559 concentration modeled at 4 mA cm^{-2} (**Fig. 6(a)**) against 0.4 mA cm^{-2} (**Fig. 6(b)**), three remarks can
560 be made; firstly, longer time was needed to reach the peak at $r_{OH^-} = r_{CaCO_3}$. Secondly, smaller
561 concentration of interfacial CO_3^{2-} was produced at higher current density and thirdly, $CaCO_3$ electro-
562 precipitation occurred at relatively slower rate after the peak of equivalence. The involvement of gas
563 evolution might explain the described behaviors. As above-mentioned, intensified evolving H_2 gas
564 on cathode surface at higher applied current density decreased significantly the effective surface area
565 of cathode even though the OH^- production was enhanced in the meantime. Consequently, longer
566 buffer time was observed in **Fig. 4(a)** (**inset** curve) at the beginning of electrolysis in comparison to
567 **Fig. 4(b)**. Lesser amount of interfacial CO_3^{2-} was also expected at the proximity of cathode surface
568 due to the intervention of evolving gas. This disturbance on cathode took place throughout the
569 electrolysis and consequently, plausible detachment of $CaCO_3$ scaling occurred along the way. In
570 overall, slower kinetics of $CaCO_3$ deposition was observed under high current density, affirmed by
571 the trend depicted in **Fig. 4**.

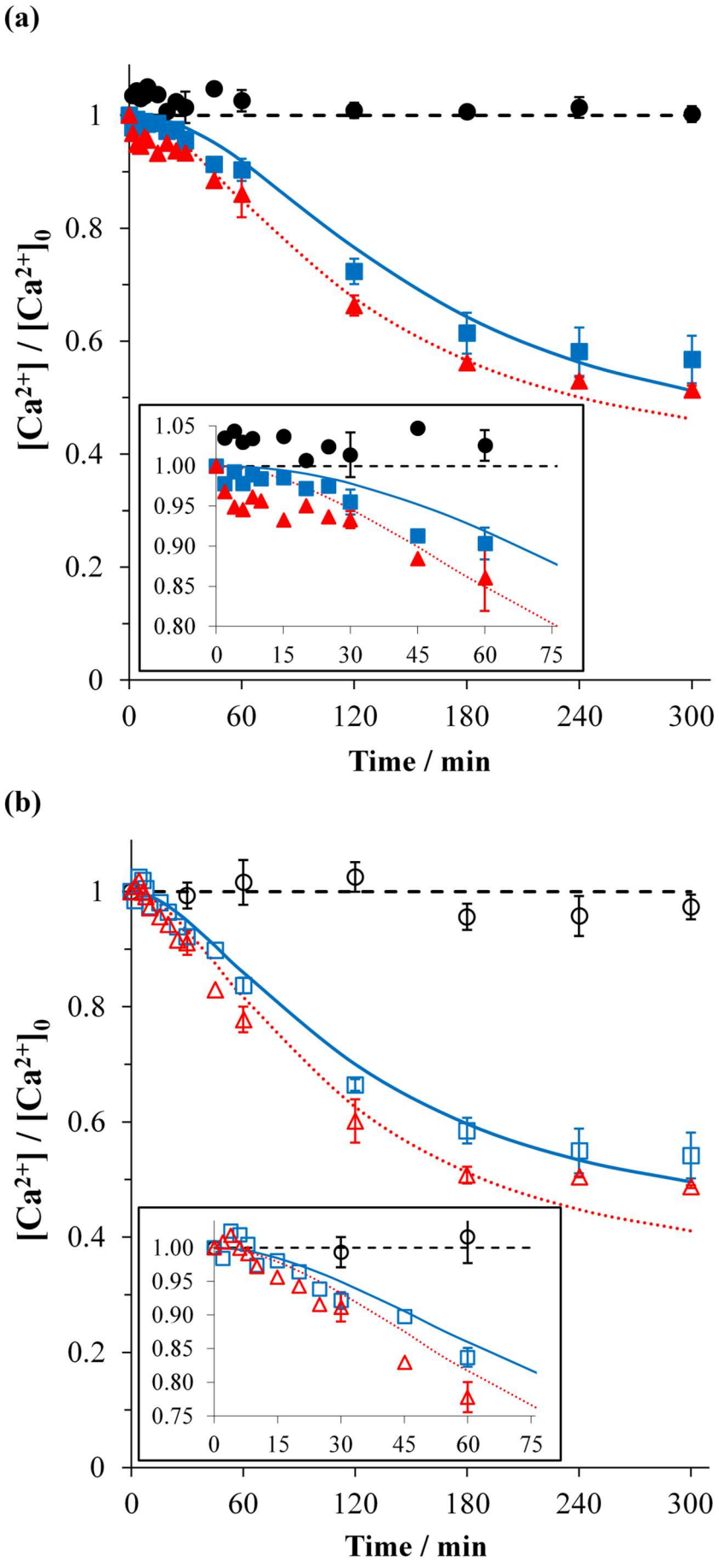

572

573 **Fig. 4**. Evolution of concentration of Ca^{2+} during the electrolysis of different matrices of electrolyte
574 (●, ○: Ca^{2+} and Mg^{2+} without CO_3^{2-}, ■, □: Ca^{2+}, Mg^{2+} and CO_3^{2-} and ▲, △: Ca^{2+} and CO_3^{2-} without
575 Mg^{2+}) at **(a)** 4 mA cm^{-2} (●, ■, ▲) and **(b)** 0.4 mA cm^{-2} (○, □, △) applied current density. (– – –):
576 model curve for Ca^{2+} and Mg^{2+} electrolyte without CO_3^{2-}, (——): model curve for Ca^{2+}, Mg^{2+} and
577 CO_3^{2-} electrolyte and (·····): model curve for Ca^{2+} and CO_3^{2-} without Mg^{2+} electrolyte. **Inset**:
578 zoom of the initial kinetic evolution of Ca^{2+}. Anode: BDD, cathode: stainless steel and inter-
579 electrode distance: 500 µm.

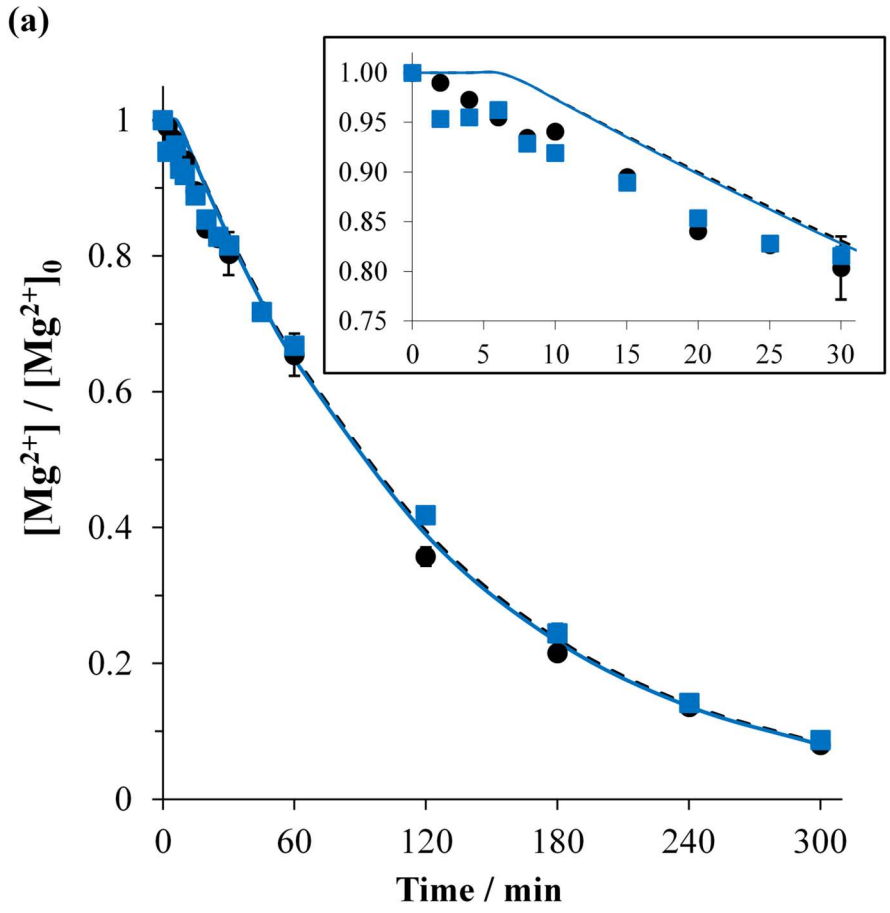
(a)
1.00
0.95
0.90
0.85
0.80
0.75
0
5
10
15
20
25
30
1
0.8
0.6
0.4
0.2
0
[Mg2+] / [Mg2+]0
0
60
120
180
240
300
Time / min

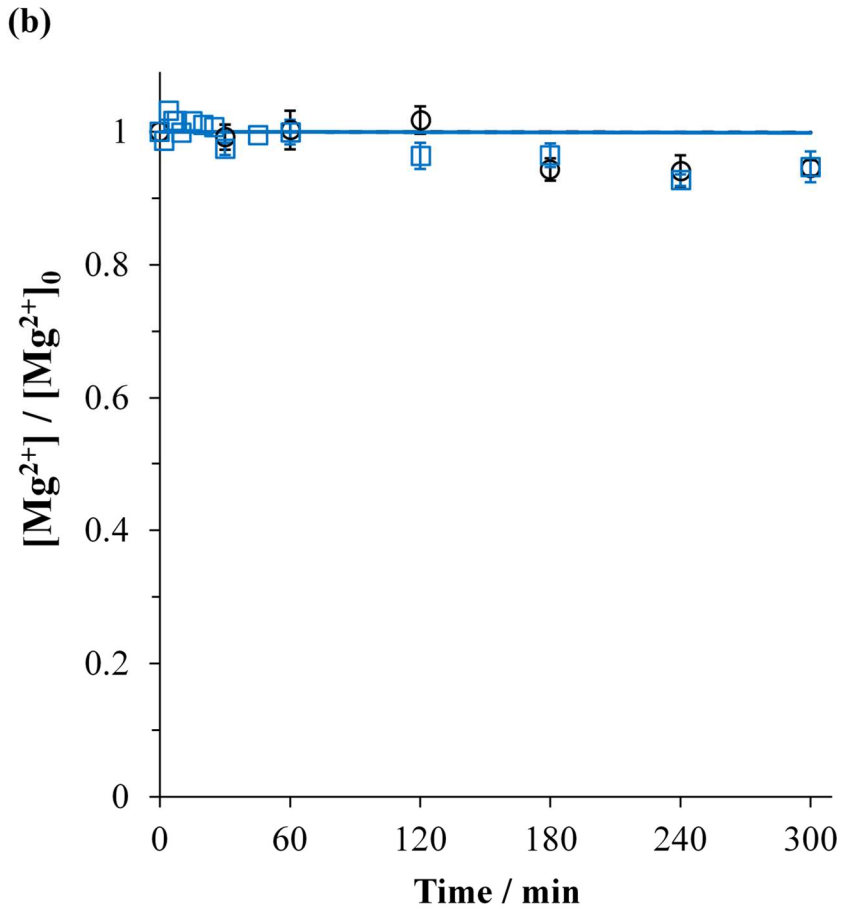
(b)
1
0.8
0.6
0.4
0.2
0
[Mg2+] / [Mg2+]0
0
60
120
180
240
300
Time / min

580

Fig. 5. Evolution of concentration of Mg^{2+} during the electrolysis of different matrices of electrolyte (●, ○: Ca^{2+} and Mg^{2+} without CO_3^{2-} and ■, □: Ca^{2+}, Mg^{2+} and CO_3^{2-}) at **(a)** 4 mA cm^{-2} (●, ■) and **(b)** 0.4 mA cm^{-2} (○, □) applied current density. (– – –): model curve for Ca^{2+} and Mg^{2+} electrolyte without CO_3^{2-} and (——): model curve for Ca^{2+}, Mg^{2+} and CO_3^{2-} electrolyte. **Inset**: zoom of the initial kinetic evolution of Mg^{2+}. Anode: BDD, cathode: stainless steel and inter-electrode distance: 500 µm.

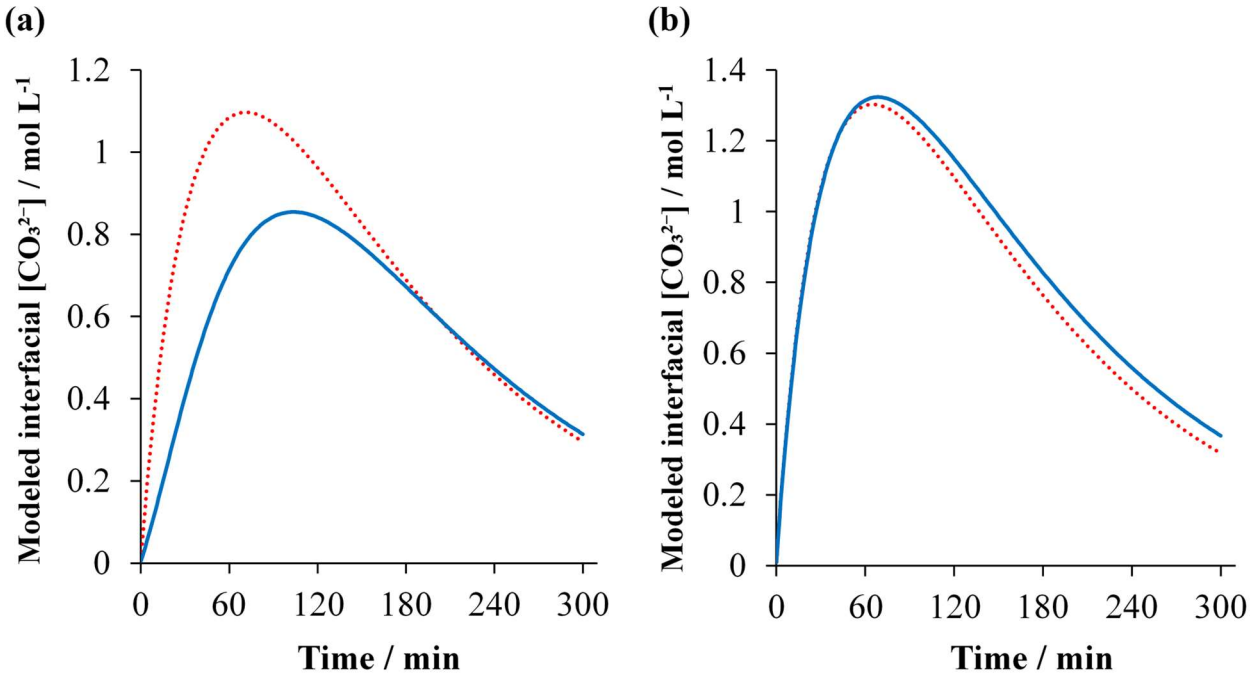

Fig. 6. Modeled concentration of interfacial CO_3^{2-} during the electrolysis of electrolyte containing Ca^{2+}, Mg^{2+} and CO_3^{2-} (——) and electrolyte containing: Ca^{2+} and CO_3^{2-} without Mg^{2+} (·····) under the polarization of **(a)** 4 mA cm^{-2} and **(b)** 0.4 mA cm^{-2} applied current density. Anode: BDD, cathode: stainless steel and inter-electrode distance: 500 µm.

4.4.2 Influence of Mg^{2+} towards the mineral electro-precipitation

To investigate the role of Mg^{2+} towards $CaCO_3$ deposition in microfluidic reactor, two electrolytes, both consisting of Ca^{2+} and CO_3^{2-} but only one contained Mg^{2+}, were compared. According to **Fig. 4**, at both applied current densities, concentrations of Ca^{2+} decreased over time. In both cases, higher degree of $CaCO_3$ electro-precipitation (12%) was observed in the system in absence of Mg^{2+}. This

difference was even more significant when the electrochemical cell was polarized with lower current density where the interface was less perturbed by evolving gas (**Fig. 4(b)**). This finding can be attributed to the inhibition effect of Mg^{2+} during $CaCO_3$ deposition **[25, 30, 34, 42, 49]**. Mg^{2+} can either incorporate into the $CaCO_3$ lattices lowering their growth kinetics on cathode surface **[25, 49, 80]**, or, a thin layer of magnesian gel-like film **[42, 70, 81]** - which was formed prior to the $CaCO_3$ deposition **[37, 81]** - partially limited the surface reactivity of cathode towards the scaling of $CaCO_3$. Nonetheless, it has been reported that $CaCO_3$ crystal can still develop and grow on the layer of $Mg(OH)_2$ as confirmed by mixture of brucite and aragonite crystals from microscopic techniques **[42, 81-83]**. With regard to the competing reaction of gas evolution on the surface of cathode at higher current density, it remained true while working with electrolyte without Mg^{2+}. More intense H_2 gas evolution led to less $CaCO_3$ electro-precipitation (**Fig. 4**) as previously described. A slight difference was found in terms of $CaCO_3$ crystallography according to literature. When cathode potential was relatively low in the region of solvent reduction, $CaCO_3$ deposit has been reported to crystallize under cubic calcite allotropy. Whilst in presence of Mg^{2+}, $CaCO_3$ takes aragonite form **[18, 23, 37, 42, 62]**. Under strong evolving gas activity, porous structure of $CaCO_3$ deposit has been reported **[35-37, 43, 84]**.

In addition, the trends of modeled interfacial CO_3^{2-} depicted on **Fig. 6** complement the deduction made on the inhibiting role of Mg^{2+} towards $CaCO_3$ electro-precipitation. At higher applied current density (4 mA cm^{-2}, **Fig. 6(a)**), $Mg(OH)_2$ deposit was formed in the electrolyte containing Mg^{2+}. The formation of $Mg(OH)_2$ deposit partly consumed interfacial OH^-. As a result, r_{OH^-} decreased as accounted in the model (**Eq. (23)**). Together with H_2 gas evolution at higher current polarization, the increment of interfacial CO_3^{2-} concentration was slower in the electrolyte in presence of Mg^{2+} relatively to the one without Mg^{2+}. Smaller interfacial CO_3^{2-} concentration was expected at cathode surface therefore lowering kinetic rate of $CaCO_3$ electro-precipitation. Contrastingly, $Mg(OH)_2$ electro-precipitation did not take place at lower current density. Gas evolution was significantly lower at 0.4 mA cm^{-2}. Consequently, the evolution of modeled interfacial CO_3^{2-} concentrations (**Fig. 6(b)**)

for both electrolytes in absence and presence of Mg^{2+} were quite similar. It means that the availability of interfacial CO_3^{2-} on cathode surface was about the same for either electrolyte. Hence, it was then confirmed from **Fig. 4(b)** that the lower growth rate of $CaCO_3$ deposition obtained in the presence of Mg^{2+} at lower current density was due to the decrease of supersaturation degree of $CaCO_3$ in the presence of Mg^{2+} **[85]**. As previously discussed, it can adsorb or incorporate into $CaCO_3$ crystal lattice inhibiting its growth during the electrolysis **[49, 80]**.

4.4.3 Influence of Ca^{2+} towards the mineral electro-precipitation

Fig. 7 illustrates the behavior of mineral deposition during electrolysis in the presence or absence of Ca^{2+} at 4 and 0.4 mA cm^{-2}. From **Fig. 7(a)**, it was observed that Mg^{2+} underwent electro-precipitation independently of Ca^{2+}. The evolution of concentration of Mg^{2+} in presence of Ca^{2+} followed exactly the trend given in absence of Ca^{2+}. This observation indicated indifferent role of Ca^{2+} towards the deposition of Mg^{2+}. From **Fig. 7(b)**, it was noticed that Mg^{2+} did not precipitate at lower applied current density (0.4 mA cm^{-2}) in both matrices of electrolyte. The evolution of TIC in **Fig. S2(e-f)** suggested that the concentration of CO_3^{2-} declined negligibly over time in the matrix without Ca^{2+} relatively to the behavior in the presence of Ca^{2+}. This tendency coupled with the observation made in **Fig. 7(a)** allowed deducing on the absence of electro-precipitation of $MgCO_3$ in our operated microfluidic cell configuration. In addition, considering the fact that CO_3^{2-} did not precipitate in the absence of Ca^{2+}, the results in this section corroborated with those in section **4.4.1** in which CO_3^{2-} only underwent precipitation with Ca^{2+} to form $CaCO_3$ deposit. The evolution of modeled interfacial CO_3^{2-} concentration in the case without Ca^{2+} plotted in **Figs. 7(c)** and **7(d)** might as well come into similar conclusion. Interfacial CO_3^{2-} concentration increased in conjunction to OH^- production on electrode surface. No CO_3^{2-} was consumed at the vicinity of cathode in the absence of Ca^{2+} allowing a continuous and quicker shift into CO_3^{2-} form at cathode interface. The interfacial CO_3^{2-} concentration arrived at a quasi-plateau at the end of electrolysis when the majority of carbon was

converted into CO_3^{2-} form. Slower rate of OH^- production at higher applied current was due to involvement of H_2 evolution activity.

To summarize, Mg^{2+} deposited under the form of $Mg(OH)_2$ and it was not influenced by the presence of Ca^{2+} nor CO_3^{2-}. Only applied current density influenced the electro-precipitation of $Mg(OH)_2$ as already described in section **4.4.1**. According to Bénézeth et al. **[52]**, $MgCO_3$ or commonly known as magnesite, possesses very slow kinetics of crystallization. Other hydrated Mg-carbonates forms are plausible owing to slow precipitation kinetics of the former, but they are rather unstable due to strong hydrated character of Mg^{2+} **[52, 86, 87]**. As a result, direct electro-precipitation of $MgCO_3$ would be realizable but only under stringent conditions, i.e. elevated departing supersaturated solution, elevated temperature and very high CO_2 partial pressure **[88]**. Hence, based on our experimental results supported by the work of other authors, $MgCO_3$ was not formed under our experimental conditions.

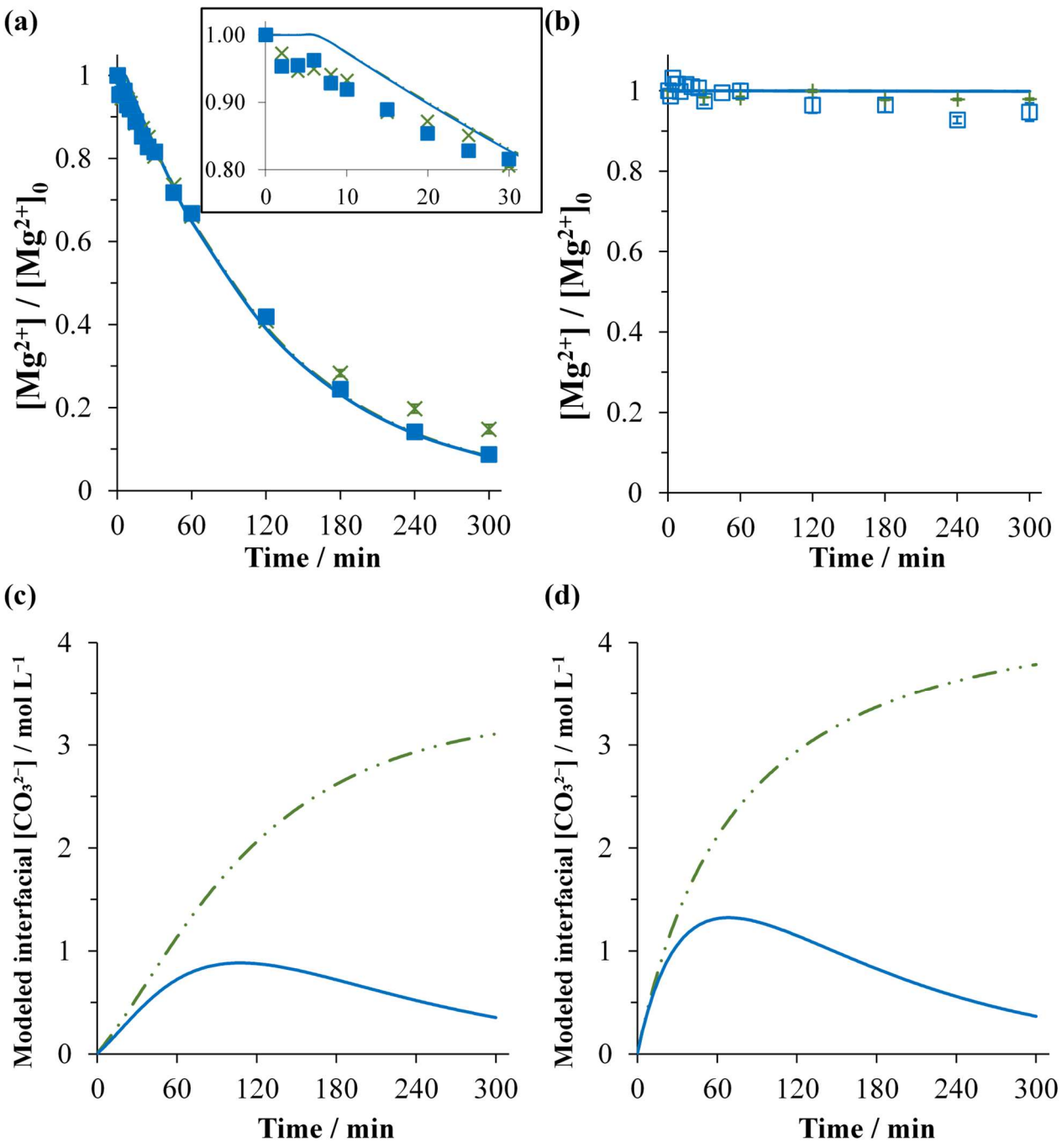

658

659 **Fig. 7**. Evolution of Mg^{2+} (**a**, **b**) and modeled interfacial CO_3^{2-} (**c**, **d**) concentrations during the
660 electrolysis of electrolyte containing Ca^{2+} (■, □) or without Ca^{2+} (×, +) at 4 mA cm^{-2} (**a**, **c**) and 0.4
661 mA cm^{-2} (**b**, **d**). Model curves of electrolyte in presence of Ca^{2+} (——) or in absence of Ca^{2+} (
662 — · ·). **Inset (a)**: zoom of the initial kinetics evolution of Mg^{2+}. Anode: BDD, cathode: stainless
663 steel and inter-electrode distance: 500 µm.

664

665 **4.4.4 Evolution of pH and conductivity**

666 In **Fig. S3** are plotted the graphs of variation of bulk solution pH and ionic conductivity throughout
667 the electrolysis of all investigated matrices of electrolyte at both high and low applied current
668 densities. Few general trends can be drawn from these curves. Firstly, solution pH and ionic
669 conductivity tended to decrease in the bulk during the electro-precipitation process. The decrease in
670 pH was the most remarkable in the electrolyte without carbonates since no buffer effect of HCO_3^-
671 /CO_3^{2-} was present in this matrix. Similar remark was also made by other authors, Tlili et al. **[64]** and
672 Piri et al. **[43]**, when they checked upon the variation of pH in bulk solution during the formation of
673 $CaCO_3$. This drop of pH value was ascribed to the consumption of OH^- that partake in the reaction of
674 $Mg(OH)_2$ deposition according to **Eq. (3)**. It could also be attributed to the pH participation towards
675 the thermodynamic equilibrium shift of HCO_3^-/CO_3^{2-} in favor of CO_3^{2-} formation in **Eq. (5)**, while
676 consuming OH^-. Net concentration of OH^- in the bulk therefore declined, indicated by the decrease
677 of measured bulk pH. The only case where bulk pH did not decrease was during the electrolysis of
678 electrolyte in absence of Ca^{2+}. At both applied current densities, $CaCO_3$ deposit was not formed.
679 Meanwhile, OH^- was continuously electro-generated on the surface of cathode. OH^- diffusing from
680 cathode surface to the bulk only reacted with existing HCO_3^- until complete conversion into the basic
681 form, i.e. CO_3^{2-}(**Eq. (5)**). Then, the accumulation of OH^- in the bulk yielded in an increase of pH
682 value. Moreover, the only electro-precipitation that occurred in the electrolyte in absence of Ca^{2+} was
683 $Mg(OH)_2$ and it was only seen at higher range of applied current density. However, as demonstrated
684 in **Fig. S3(a)**, OH^- consumed for the deposition of $Mg(OH)_2$ on cathode surface contributed trivially
685 towards the diminishing pattern of pH in the bulk unlike during the deposition of $CaCO_3$.

686 Similar argument can be done towards the trend of ionic conductivity in the bulk. Knowing the fact
687 that OH^- possesses high value of ionic conductivity despite not being the highest relatively to H^+, its
688 consumption throughout the electro-precipitation event of $CaCO_3$ manifested a decline in overall bulk
689 ionic conductivity as shown in **Fig. S3(c)** and **Fig. S3(d)**.

690 **4.4.5 Mass balance and elements recovery**

691 **Fig. 8** depicts the recovery of Mg and Ca from the different electrochemical reactor compartments at
692 the end of experiment for different matrices of electrolyte at both current densities investigated. Very
693 high percentage of Mg and Ca recovery across all experiments was verified with the lowest being
694 90%. The percentage of recovery across all electrolysis took an average value of 95%. From **Fig. 8**,
695 in the case where electro-precipitation occurred, high percentage of Mg and Ca were recovered from
696 cathode while negligible quantity was found in tubing and from anode surface. It is important to note
697 that high Mg and Ca recovery means negligible loss of the elements was ensured. Mass balance of
698 Mg and Ca from different compartment was conserved. Consequently, the trends of cation
699 concentrations depicted in previous figures were reliable. Their decay from electrolyte bulk, coupled
700 to high mass recovery from cathode surface was indicative of mineral precipitations occurring on the
701 cathode.

702 Looking at **Fig. 8(b)**, percentages of mass of Ca recovered from cathode in both matrices of
703 electrolyte were higher at 0.4 mA cm^{-2} as compared to 4 mA cm^{-2}, confirming the relative influence
704 of evolving gas activity on cathode surface. Moreover, the percentage of Ca recovery from cathode
705 was always lower in the matrix in presence of Mg^{2+}, whatever the current density applied. It is in
706 agreement with the fact that less Ca^{2+} was electro-precipitated in presence of Mg^{2+} demonstrating the
707 inhibition effect of the latter towards $CaCO_3$ co-precipitation with $Mg(OH)_2$.

708 On the other hand, the recovery of Mg in all electrolytes under study illustrated in **Fig. 8(a)** confirmed
709 that the Mg^{2+}-based deposit only took place under high current density. It further corroborated the
710 fact that the formation of $Mg(OH)_2$ deposit was not influenced by other ionic species co-present in
711 the electrolyte.

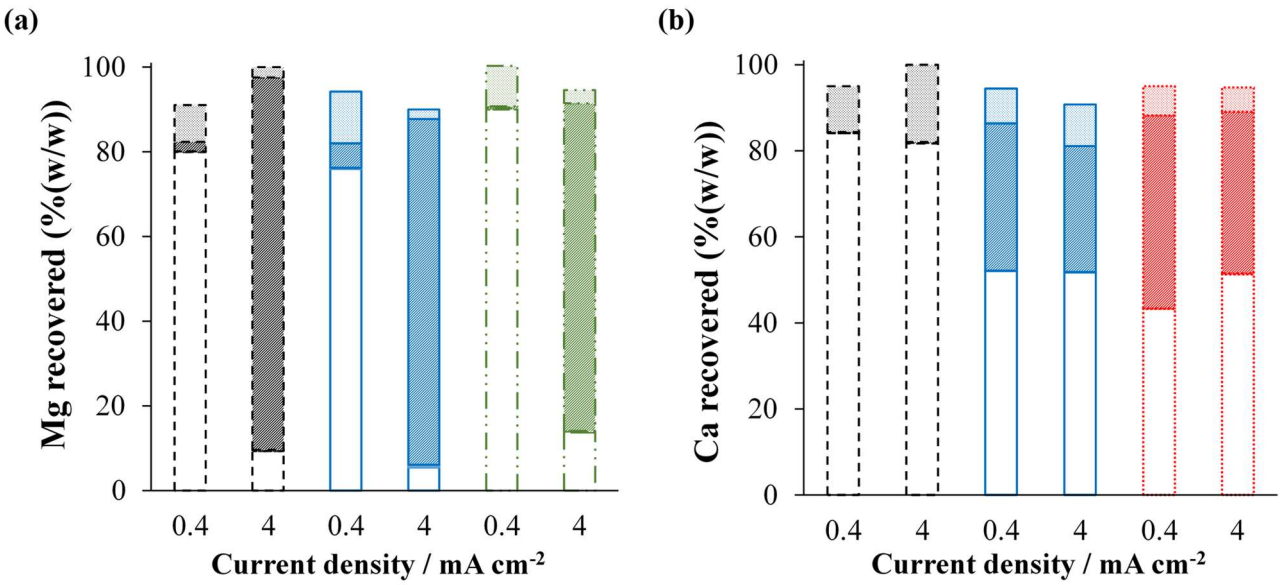

712

713 **Fig. 8**. Percentages (w/w) of **(a)** Mg and **(b)** Ca recovered from different parts of experimental pilot
714 (□: electrolyte, ▨: cathode, ⊞: anode and ⊡: tube) after 300 min-electrolysis at 0.4 and 4 mA cm^{-2}
715 of different matrices of electrolyte ((- - - - -): Ca^{2+} and Mg^{2+} without CO_3^{2-}, (———): Ca^{2+}, Mg^{2+}
716 and CO_3^{2-}, (·····): Ca^{2+} and CO_3^{2-} without Mg^{2+}, and (— · — · —): Mg^{2+} and CO_3^{2-} without Ca^{2+}).

717 **4.4.6 Theoretical evolution of Ca^{2+}, Mg^{2+} and interfacial CO_3^{2-} during electrolysis in different**
718 **matrices**

719 Simulations of evolution of Mg^{2+} concentration during the electrolysis of all matrices of electrolyte
720 depicted in **Fig. 5(a)**, **Fig. 5(b)**, **Fig. 7(a)** and **Fig. 7(b)** fitted very well with their corresponding
721 experimental curves. Their RMSE values stayed underneath 0.0078 as summarized in **Table S2** whilst
722 ME and IOA values remained above 0.9849 and 0.9956 respectively under all case study. The
723 modelling indicated that under the polarization of 4 mA cm^{-2}, it took approximately 7 min for the
724 electrochemical system to reach interfacial OH^-_{crit} (0.16 mol m^{-3}, interfacial pH_{crit} = 10.2) before Mg^{2+}
725 starting to precipitate. This lag time was also observed experimentally as illustrated in **inset** of **Fig.**
726 **5(a)** and **Fig. 7(a)**. The model of Mg^{2+} concentrations decreased over time following the calibrated
727 empirical value of $k_{Mg(OH)_2}$ of 0.330 m^6 mol^{-2} min^{-1}. Exactly same trend was observed across all
728 matrices of electrolyte containing Mg^{2+} since $Mg(OH)_2$ deposition was independent of CO_3^{2-} and Ca^{2+}

ions. Accordingly, similar procedures were carried out for $Ca(OH)_2$ deposit. However, due to high solubility of $Ca(OH)_2$, the OH_{crit}^- concentration that needed to be reached was as high as 36.6 mol m^{-3} (pH = 12.6). Under our investigated experimental setup, this OH_{crit}^- value was not achieved by either applied current density. Maximum theoretical interfacial OH^- concentration was obtained under 4 mA cm^{-2} at 7.43 mol m^{-3} (pH = 11.8). As a consequence, no precipitation of $Ca(OH)_2$ was observed.

The modelling of interfacial CO_3^{2-} concentration at cathode surface was rather accurate as extensively discussed in section **4.4.1** to **4.4.3**. In agreement to **Eq. (20)** and **Eq. (23)**, interfacial CO_3^{2-} was proven to be dependent on applied current density; hence H_2 gas evolution activity on cathode. Its concentration was as well influenced by the consumption of interfacial OH^-. Taking into account these matters, **Eq. (21)** yields reliable models of evolution of Ca^{2+} concentration across multiple matrices of electrolyte investigated. The calibrated empirical value of constant rate of $CaCO_3$ electro-precipitation (k_{CaCO_3}) was 3.6 × 10^{-3} m^3 mol^{-1} min^{-1}. Ca^{2+} model curves fitted their experimental counterparts well. In agreement to listed values in **Table S2**, the lowest RMSE was 0.0761 in the system containing Mg^{2+}, Ca^{2+} and CO_3^{2-} at low applied current density. Other RMSE values ranged from 0.0828 to 0.1163 and the Ca^{2+} model fitting remained reliable in accordance to other model fitting criteria such as ME and IOA. Their respective values obtained for the case with worst RMSE fitting (i.e. matrix containing Ca^{2+} and CO_3^{2-} without Mg^{2+} at 0.4 mA cm^{-2}) were 0.9758 and 0.9934.

In order to account for intensive concomitant H_2 gas evolution at high applied current density, the corrective term α introduced in **Eq. (10)** and **Eq. (23)** was taken at 7.5% to fit experimental results. This tells that approximately only 7.5% of cathode surface was effective for mineral electro-precipitation including the detachment of deposits already formed by the evolving gas. The α value was found to approximately match the observed experimental decrease of $CaCO_3$ scaling (7.2%) between the two regions of applied current densities investigated. In addition, it has also been observed that at lower applied current, the applied current density already surpassed limiting current density (section **4.3**). This means that secondary reaction like concurrent gas evolution was already

present but it did not influence on the availability of interfacial CO_3^{2-} on cathode (**Fig. 6(b)**) but rather improving the mass transport of Ca^{2+} and Mg^{2+} towards cathode surface (section **4.4.1**). The hindrance of $CaCO_3$ growth kinetics in this case was purely attributed to steric inhibition of Mg^{2+} in solution since no $Mg(OH)_2$ was produced under this condition **[81]**. Therefore, the kinetic law of depositing $CaCO_3$ was slightly modified taking into account this effect as defined in **Eq. (32)**:

$$r_{Ca^{2+}} = -r_{CaCO_3} = -(k_{CaCO_3} - k_{inhib})\,[Ca^{2+}][CO_3^{2-}]_{int,t} \quad (32)$$

where k_{inhib} (in m^3 mol^{-1} min^{-1}) is the steric inhibition of Mg^{2+} ion either by adsorption or incorporation into $CaCO_3$ lattices as previously discussed in section **4.4.2**. By fitting the modeled Ca^{2+} concentration with its experimental data (the matrix in presence of Mg^{2+}) at low applied current density, k_{inhib} was evaluated to be 9.0×10^{-4} m^3 mol^{-1} min^{-1}. This value is about 25% of the empirical $CaCO_3$ electro-precipitation constant of k_{CaCO_3}. It suggests that in the presence of 5 mg L^{-1} of Mg^{2+} (in the system containing 150 mg L^{-1} of Ca^{2+}), 25% less $CaCO_3$ electro-precipitation should have been observed due to the inhibition effect. However, experimental results indicated only 12% less $CaCO_3$ scaling after 5 hours of electrolysis, which is about half the theoretical value. This discrepancy was attributed to the enhancement of Ca^{2+}, CO_3^{2-} and Mg^{2+} transport by micro- and macro-convection towards cathode interface **[73-76]** which could favor the electro-precipitation reactions.

5. Conclusions

The occurrence of mineral electro-precipitation inside a microfluidic reactor was newly investigated in this work. Due to the existence of precipitating agents in water resources of natural or anthropogenic origin, electro-precipitates can be formed during advanced electro-oxidation processes and they might compromise the efficiency of such processes. Inside a scalable microfluidic reactor equipped with BDD, the phenomenon of local alkalization on cathode surface originated principally from reduction of water and not dissolved O_2 under investigated conditions. The reaction kinetics at the proximity of cathode surface were limited by mass transport. Upon further investigation, the

778 influence of electromigration towards the occurrence of electro-precipitation was negligible, meaning
779 that diffusion was the main limiting factor.

780 $MgCO_3$ deposit was not observed throughout this work, while $Mg(OH)_2$ precipitate was highly
781 dependent on applied current density, because the local pH value was the decisive parameter upon its
782 formation. Thus $Mg(OH)_2$ was hardly formed at low applied current density. In addition, $Mg(OH)_2$
783 deposition was independent of ionic species jointly present in the electrolyte bulk. Regarding Ca-
784 based precipitates, $Ca(OH)_2$ was not formed under our investigated configuration, while $CaCO_3$ was
785 easily deposited on the surface of cathode even under small current polarization. More electro-
786 precipitation of $CaCO_3$ was recovered at lower current density (0.4 mA cm^{-2}) owing to vigorous gas
787 evolution at higher applied current density (4 mA cm^{-2}). $CaCO_3$ scaling was proven to be impeded by
788 the presence of Mg^{2+} ion. A novel mathematical model was proposed to simulate and predict the
789 evolution of depositing species of Mg^{2+}, Ca^{2+} and interfacial CO_3^{2-} in presence or absence of co-
790 deposition within the microfluidic reactor. The models fitted well with experimental data given the
791 RMSE, ME and IOA values.

792 It could be deduced eventually that $^{\bullet}OH$ continuously produced on BDD anode did not influence
793 towards the electro-precipitation occurring on cathode counterpart in the applied condition despite
794 micrometric distance separating them. In order to minimize scaling formation, a compromise with
795 respect to degradation efficiency of pollutant needs to be accommodated for upcoming research.
796 Lower applied current density could be used, but lower degradation of pollutant via direct electron
797 transfer or indirect oxidation would be consequently expected due to lower overpotential.
798 Alternatively, mineral electro-precipitation could be minimized by applying high current density,
799 benefiting the intensified evolving gas on cathode surface to un-do the deposits. However, energy
800 consumption would be deemed deal-breaker for its application at industrial scale. Nonetheless, since
801 micrometric range of inter-electrode distance extensively cut down the internal resistance of
802 electrochemical cells, cell voltage would not be eventually so high at such high current densities.

803 Further studies are required to test microfluidic configuration in order to concomitantly yield high
804 degradation efficiency while minimizing the resulting mineral electro-precipitation.

805 **Acknowledgments**

806 Authors would like to express their gratitude to French ministry of higher education and research
807 (MESRI) for financial funding of doctoral contract of Faidzul Hakim Adnan as well as financial
808 support received from Carnot ICEEL, LTSER Zone Atelier du bassin de la Moselle (ZAM) and
809 European regional development fund program (CPER SusChemProc).

References

[1] S.D. Richardson, S.Y. Kimura, Water analysis: Emerging contaminants and current issues, Analytical Chemistry, 88 (2016) 546-582.

[2] B. Petrie, R. Barden, B. Kasprzyk-Hordern, A review on emerging contaminants in wastewaters and the environment: Current knowledge, understudied areas and recommendations for future monitoring, Water Research, 72 (2015) 3-27.

[3] M.A. Oturan, J.-J. Aaron, Advanced oxidation processes in water/wastewater treatment: Principles and applications. A review, Critical Reviews in Environmental Science and Technology, 44 (2014) 2577-2641.

[4] H. Monteil, Y. Péchaud, N. Oturan, M.A. Oturan, A review on efficiency and cost effectiveness of electro-and bio-electro-fenton processes: Application to the treatment of pharmaceutical pollutants in water, Chemical Engineering Journal, 376 (2019) 119577.

[5] C.A. Martínez-Huitle, M.A. Rodrigo, I. Sirés, O. Scialdone, Single and coupled electrochemical processes and reactors for the abatement of organic water pollutants: A critical review, Chemical Reviews, 115 (2015) 13362-13407.

[6] F.C. Moreira, R.A.R. Boaventura, E. Brillas, V.J.P. Vilar, Electrochemical advanced oxidation processes: A review on their application to synthetic and real wastewaters, Applied Catalysis B: Environmental, 202 (2017) 217-261.

[7] E. Mousset, N. Oturan, M.A. Oturan, An unprecedented route of OH radical reactivity evidenced by an electrocatalytical process: Ipso-substitution with perhalogenocarbon compounds, Applied Catalysis B: Environmental, 226 (2018) 135-146.

[8] E. Mousset, Y. Pechaud, N. Oturan, M.A. Oturan, Charge transfer/mass transport competition in advanced hybrid electrocatalytic wastewater treatment: Development of a new current efficiency relation, Applied Catalysis B: Environmental, 240 (2019) 102-111.

[9] P.V. Nidheesh, G. Divyapriya, N. Oturan, C. Trellu, M.A. Oturan, Environmental applications of boron-doped diamond electrodes: 1. Applications in water and wastewater treatment, ChemElectroChem, 6 (2019) 2124-2142.

[10] O. Scialdone, A. Galia, C. Guarisco, S. Randazzo, G. Filardo, Electrochemical incineration of oxalic acid at boron doped diamond anodes: Role of operative parameters, Electrochimica Acta, 53 (2008) 2095-2108.

[11] O. Scialdone, E. Corrado, A. Galia, I. Sirés, Electrochemical processes in macro and microfluidic cells for the abatement of chloroacetic acid from water, Electrochimica Acta, 132 (2014) 15-24.

[12] O. Scialdone, A. Galia, S. Sabatino, D. Mira, C. Amatore, Electrochemical conversion of dichloroacetic acid to chloroacetic acid in a microfluidic stack and in a series of microfluidic reactors, ChemElectroChem, 2 (2015) 684-690.

[13] E. Mousset, Unprecedented reactive electro-mixing reactor: Towards synergy between micro- and macro-reactors?, Electrochemistry Communications, 118 (2020) 106787.

[14] J.F. Pérez, J. Llanos, C. Sáez, C. López, P. Cañizares, M.A. Rodrigo, Development of an innovative approach for low-impact wastewater treatment: A microfluidic flow-through electrochemical reactor, Chemical Engineering Journal, 351 (2018) 766-772.

[15] P. Ma, H. Ma, S. Sabatino, A. Galia, O. Scialdone, Electrochemical treatment of real wastewater. Part 1: Effluents with low conductivity, Chemical Engineering Journal, 336 (2018) 133-140.

[16] E. Mousset, M. Puce, M.N. Pons, Advanced electro-oxidation with boron-doped diamond for acetaminophen removal from real wastewater in a microfluidic reactor: Kinetics and mass-transfer studies, ChemElectroChem, 6 (2019) 2908-2916.

[17] F. Sopaj, N. Oturan, J. Pinson, F. Podvorica, M.A. Oturan, Effect of the anode materials on the efficiency of the electro-fenton process for the mineralization of the antibiotic sulfamethazine, Applied Catalysis B: Environmental, 199 (2016) 331-341.

[18] L. Beaunier, C. Gabrielli, G. Poindessous, G. Maurin, R. Rosset, Investigation of electrochemical calcareous scaling: Nuclei counting and morphology, Journal Of Electroanalytical Chemistry, 501 (2001) 41-53.
[19] C. Deslouis, D. Festy, O. Gil, G. Rius, S. Touzain, B. Tribollet, Characterization of calcareous deposits in artificial sea water by impedance techniques — 1. Deposit of $CaCO_3$ without $Mg(OH)_2$, Electrochimica Acta, 43 (1998) 1891-1901.
[20] C. Deslouis, I. Frateur, G. Maurin, B. Tribollet, Interfacial pH measurement during the reduction of dissolved oxygen in a submerged impinging jet cell, Journal of Applied Electrochemistry, 27 (1997) 482-492.
[21] H. Deligianni, L.T. Romankiw, In situ surface pH measurement during electrolysis using a rotating pH electrode, IBM Journal of Research and Development, 37 (1993) 85-95.
[22] J. Marin-Cruz, R. Cabrera-Sierra, M. Pech-Canul, I. Gonzalez, EIS study on corrosion and scale processes and their inhibition in cooling system media, Electrochimica Acta, 51 (2006) 1847-1854.
[23] J. Marin-Cruz, E. Garcia-Figueroa, M. Miranda-Hernández, I. Gonzalez, Electrochemical treatments for selective growth of different calcium carbonate allotropic forms on carbon steel, Water Research, 38 (2004) 173-183.
[24] Y. Ben Amor, L. Bousselmi, H. Takenouti, E. Triki, Influence of sulphate ions on corrosion mechanism of carbon steel in calcareous media, Corrosion Engineering, Science and Technology, 40 (2005) 129-136.
[25] Y. Ben Amor, L. Bousselmi, B. Tribollet, E. Triki, Study of the effect of magnesium concentration on the deposit of allotropic forms of calcium carbonate and related carbon steel interface behavior, Electrochimica Acta, 55 (2010) 4820-4826.
[26] L. Bousselmi, C. Fiaud, B. Tribollet, E. Triki, Impedance spectroscopic study of a steel electrode in condition of scaling and corrosion: Interphase model, Electrochimica Acta, 44 (1999) 4357-4363.
[27] L. Bousselmi, C. Fiaud, B. Tribollet, E. Triki, The characterisation of the coated layer at the interface carbon steel-natural salt water by impedance spectroscopy, Corrosion Science, 39 (1997) 1711-1724.
[28] Z. Belarbi, B. Sotta, L. Makhloufi, B. Tribollet, J. Gamby, Modelling of delay effect of calcium carbonate deposition kinetics on rotating disk electrode in the presence of green inhibitor, Electrochimica Acta, 189 (2016) 118-127.
[29] M. Euvrard, F. Membrey, C. Filiatre, C. Pignolet, A. Foissy, Kinetic study of the electrocrystallization of calcium carbonate on metallic substrates, Journal Of Crystal Growth, 291 (2006) 428-435.
[30] C. Deslouis, D. Festy, O. Gil, V. Maillot, S. Touzain, B. Tribollet, Characterization of calcareous deposits in artificial sea water by impedances techniques: 2-deposit of $Mg(OH)_2$ without $CaCO_3$, Electrochimica Acta, 45 (2000) 1837-1845.
[31] R. Jaouhari, A. Benbachir, A. Guenbour, C. Gabrielli, J. Garcia-Jareno, G. Maurin, Influence of water composition and substrate on electrochemical scaling, Journal of The Electrochemical Society, 147 (2000) 2151.
[32] A. Martinod, A. Neville, M. Euvrad, K. Sorbie, Electrodeposition of a calcareous layer: Effects of green inhibitors, Chemical Engineering Science, 64 (2009) 2413-2421.
[33] C. Deslouis, P. Falaras, O. Gil, M. Jeannin, V. Maillot, B. Tribollet, Influence of clay on calcareous deposit in natural and artificial sea water, Electrochimica Acta, 51 (2006) 3173-3180.
[34] S.-H. Lin, S.C. Dexter, Effects of temperature and magnesium ions on calcareous deposition, Corrosion, 44 (1988) 615-622.
[35] J. Marin-Cruz, R. Cabrera-Sierra, M. Pech-Canul, I. Gonzalez, Characterization of different allotropic forms of calcium carbonate scales on carbon steel by electrochemical impedance spectroscopy, Journal of Applied Electrochemistry, 34 (2004) 337-343.
[36] S.M. Hoseinieh, T. Shahrabi, Influence of ionic species on scaling and corrosion performance of AISI 316L rotating disk electrodes in artificial seawater, Desalination, 409 (2017) 32-46.
[37] S.M. Hoseinieh, T. Shahrabi, B. Ramezanzadeh, M.F. Rad, The role of porosity and surface morphology of calcium carbonate deposits on the corrosion behavior of unprotected API 5L X52

910 rotating disk electrodes in artificial seawater, Journal of The Electrochemical Society, 163 (2016)
911 C515-C529.
912 [38] F. Sopaj, N. Oturan, J. Pinson, F.I. Podvorica, M.A. Oturan, Effect of cathode material on electro-
913 fenton process efficiency for electrocatalytic mineralization of the antibiotic sulfamethazine,
914 Chemical Engineering Journal, 384 (2020) 123249.
915 [39] S. Mathé, Chimie des solutions, Dunod2018.
916 [40] W.M. Haynes, CRC Handbook of chemistry and physics, 97th ed., CRC press, 2017.
917 [41] H. Vogt, R.J. Balzer, The bubble coverage of gas-evolving electrodes in stagnant electrolytes,
918 Electrochimica Acta, 50 (2005) 2073-2079.
919 [42] C. Barchiche, C. Deslouis, D. Festy, O. Gil, P. Refait, S. Touzain, B. Tribollet, Characterization
920 of calcareous deposits in artificial seawater by impedance techniques: 3 — deposit of $CaCO_3$ in the
921 presence of Mg(II), Electrochimica Acta, 48 (2003) 1645-1654.
922 [43] M. Piri, R. Arefinia, Investigation of the hydrogen evolution phenomenon on $CaCO_3$
923 precipitation in artificial seawater, Desalination, 444 (2018) 142-150.
924 [44] O. Scialdone, A. Galia, S. Sabatino, Electro-generation of H_2O_2 and abatement of organic
925 pollutant in water by an electro-fenton process in a microfluidic reactor, Electrochemistry
926 Communications, 26 (2013) 45-47.
927 [45] J. Newman, K.E. Thomas-Alyea, Electrochemical systems, 3rd ed., John Wiley & Sons, 2012.
928 [46] O. Velts, M. Uibu, J. Kallas, R. Kuusik, CO_2 mineral trapping: Modeling of calcium carbonate
929 precipitation in a semi-batch reactor, Energy Procedia, 4 (2011) 771-778.
930 [47] S.J. Kakaraniya, A. Mehra, Reactive precipitation in gas−liquid systems, Industrial &
931 Engineering Chemistry Research, 46 (2007) 1125-1137.
932 [48] C. Kazadi Mbamba, D.J. Batstone, X. Flores-Alsina, S. Tait, A generalised chemical
933 precipitation modelling approach in wastewater treatment applied to calcite, Water Research, 68
934 (2015) 342-353.
935 [49] Y. Zhang, R.A. Dawe, Influence of Mg^{2+} on the kinetics of calcite precipitation and calcite
936 crystal morphology, Chemical Geology, 163 (2000) 129-138.
937 [50] M. Ben Amor, D. Zgolli, M.M. Tlili, A.S. Manzola, Influence of water hardness, substrate nature
938 and temperature on heterogeneous calcium carbonate nucleation, Desalination, 166 (2004) 79-84.
939 [51] J.N. Butler, Carbon dioxide equilibria and their applications, 1st ed., Taylor & Francis Group,
940 New York: Routledge, 1991.
941 [52] P. Bénézeth, G.D. Saldi, J.-L. Dandurand, J. Schott, Experimental determination of the solubility
942 product of magnesite at 50 to 200°C, Chemical Geology, 286 (2011) 21-31.
943 [53] P. Reichert, AQUASIM - a tool for simulation and data analysis of aquatic systems, Water
944 Science and Technology, 30 (1994) 21.
945 [54] E. Mousset, S. Pontvianne, M.-N. Pons, Fate of inorganic nitrogen species under homogeneous
946 fenton combined with electro-oxidation/reduction treatments in synthetic solutions and reclaimed
947 municipal wastewater, Chemosphere, 201 (2018) 6-12.
948 [55] C.A. Martínez-Huitle, M. Panizza, Electrochemical oxidation of organic pollutants for
949 wastewater treatment, Current Opinion in Electrochemistry, 11 (2018) 62-71.
950 [56] E. Mousset, L. Quackenbush, C. Schondek, A. Gerardin-Vergne, S. Pontvianne, S. Kmiotek, M.-
951 N. Pons, Effect of homogeneous Fenton combined with electron transfer on the fate of inorganic
952 chlorinated species in synthetic and reclaimed municipal wastewater, Electrochimica Acta, 334
953 (2020) 135608.
954 [57] E. Mousset, D.D. Dionysiou, Photoelectrochemical reactors for treatment of water and
955 wastewater: a review, Environmental Chemistry Letters, 18 (2020) 1301-1318.
956 [58] N. Vatistas, C. Comninellis, The persulfate process for the mediated oxidation of organic
957 pollutants, in: C. Comninellis, G. Chen (Eds.) Electrochemistry for the Environment, Springer New
958 York, New York, NY, 2010, pp. 229-244.
959 [59] B.P. Chaplin, Critical review of electrochemical advanced oxidation processes for water
960 treatment applications, Environmental Science: Processes & Impacts, 16 (2014) 1182-1203.

[60] B.P. Chaplin, Chapter 17 - Advantages, disadvantages, and future challenges of the use of electrochemical technologies for water and wastewater treatment, in: C.A. Martínez-Huitle, M.A. Rodrigo, O. Scialdone (Eds.) Electrochemical Water and Wastewater Treatment, Butterworth-Heinemann, 2018, pp. 451-494.
[61] A.R. Despić, Deposition and dissolution of metals and alloys. Part B: Mechanisms, kinetics, texture, and morphology, in: B.E. Conway, J.O.M. Bockris, E. Yeager, S.U.M. Khan, R.E. White (Eds.) Comprehensive Treatise of Electrochemistry: Volume 7 Kinetics and Mechanisms of Electrode Processes, Springer US, Boston, MA, 1983, pp. 451-528.
[62] H. Karoui, B. Riffault, M. Jeannin, A. Kahoul, O. Gil, M. Ben Amor, M.M. Tlili, Electrochemical scaling of stainless steel in artificial seawater: Role of experimental conditions on $CaCO_3$ and Mg(OH)2 formation, Desalination, 311 (2013) 234-240.
[63] A.J. Bard, L.R. Faulkner, Electrochemical methods: Fundamentals and applications, John Wiley & Sons2001.
[64] M.M. Tlili, M. Benamor, C. Gabrielli, H. Perrot, B. Tribollet, Influence of the interfacial pH on electrochemical $CaCO_3$ precipitation, Journal of The Electrochemical Society, 150 (2003) C765.
[65] S. Sarkar, W. Aquino, Electroneutrality and ionic interactions in the modeling of mass transport in dilute electrochemical systems, Electrochimica Acta, 56 (2011) 8969-8978.
[66] T. Li, T.C. Keener, L. Cheng, Carbon dioxide removal by using Mg(OH)2 in a bubble column: Effects of various operating parameters, International Journal of Greenhouse Gas Control, 31 (2014) 67-76.
[67] M. Panizza, P.A. Michaud, G. Cerisola, C. Comninellis, Anodic oxidation of 2-naphthol at boron-doped diamond electrodes, Journal Of Electroanalytical Chemistry, 507 (2001) 206-214.
[68] P. Cañizares, J. García-Gómez, I. Fernández de Marcos, M.A. Rodrigo, J. Lobato, Measurement of mass-transfer coefficients by an electrochemical technique, Journal Of Chemical Education, 83 (2006) 1204.
[69] R.A.W. Dryfe, 20 - Liquid junction potentials, in: C.G. Zoski (Ed.) Handbook of Electrochemistry, Elsevier, Amsterdam, 2007, pp. 849-877.
[70] C. Barchiche, C. Deslouis, O. Gil, P. Refait, B. Tribollet, Characterisation of calcareous deposits by electrochemical methods: Role of sulphates, calcium concentration and temperature, Electrochimica Acta, 49 (2004) 2833-2839.
[71] T. Okstad, Ø. Rannestad, R. Johnsen, K. Nisancioglu, Significance of hydrogen evolution during cathodic protection of carbon steel in seawater, Corrosion, 63 (2007) 857-865.
[72] C. Arkam, Quartz crystal electrogravimetry with controlled hydrodynamics, Journal of The Electrochemical Society, 141 (1994) L103.
[73] H. Vogt, The role of single-phase free convection in mass transfer at gas evolving electrodes — 1. Theoretical, Electrochimica Acta, 38 (1993) 1421-1426.
[74] H. Vogt, Gas-evolving electrodes, in: E. Yeager, J.O.M. Bockris, B.E. Conway, S. Sarangapani (Eds.) Comprehensive Treatise of Electrochemistry: Electrodics: Transport, Springer US, Boston, MA, 1983, pp. 445-489.
[75] L.J.J. Janssen, Behaviour of and mass transfer at gas-evolving electrodes, Electrochimica Acta, 34 (1989) 161-169.
[76] M.G. Fouad, G.H. Sedahmed, Mass transfer at gas evolving screen electrodes, Electrochimica Acta, 20 (1975) 615-618.
[77] C. Gabrielli, G. Maurin, G. Poindessous, R. Rosset, Nucleation and growth of calcium carbonate by an electrochemical scaling process, Journal Of Crystal Growth, 200 (1999) 236-250.
[78] Y. Ben Amor, L. Bousselmi, M.C. Bernard, B. Tribollet, Nucleation-growth process of calcium carbonate electrodeposition in artificial water — influence of the sulfate ions, Journal Of Crystal Growth, 320 (2011) 69-77.
[79] T. Chen, A. Neville, M. Yuan, Calcium carbonate scale formation — assessing the initial stages of precipitation and deposition, Journal of Petroleum Science and Engineering, 46 (2005) 185-194.
[80] M. Kitamura, Crystallization and transformation mechanism of calcium carbonate polymorphs and the effect of magnesium ion, Journal Of Colloid And Interface Science, 236 (2001) 318-327.

[81] K.E. Mantel, W.H. Hartt, T.-Y. Chen, Substrate, surface finish, and flow rate influences on calcareous deposit structure, Corrosion, 48 (1992) 489-500.
[82] C. Gabrielli, Quartz crystal microbalance investigation of electrochemical calcium carbonate scaling, Journal of The Electrochemical Society, 145 (1998) 2386.
[83] S. Xu, Structure and morphology of electrodeposited $CaCO_3$: X-ray diffraction and microscopy studies, Journal of The Electrochemical Society, 146 (1999) 3315.
[84] C. Gabrielli, M. Keddam, A. Khalil, R. Rosset, M. Zidoune, Study of calcium carbonate scales by electrochemical impedance spectroscopy, Electrochimica Acta, 42 (1997) 1207-1218.
[85] H.J. Meyer, The influence of impurities on the growth rate of calcite, Journal Of Crystal Growth, 66 (1984) 639-646.
[86] F.L. Sayles, W.S. Fyfe, The crystallization of magnesite from aqueous solution, Geochimica et Cosmochimica Acta, 37 (1973) 87-99.
[87] L. Hopkinson, K. Rutt, G. Cressey, The transformation of nesquehonite to hydromagnesite in the system CaO-MgO-H_2O-CO_2: An experimental spectroscopic study, The Journal of Geology, 116 (2008) 387-400.
[88] M. Hänchen, V. Prigiobbe, R. Baciocchi, M. Mazzotti, Precipitation in the Mg-carbonate system — effects of temperature and CO_2 pressure, Chemical Engineering Science, 63 (2008) 1012-1028.